Supporting Information

Highly Dense Atomic Fe-Ni Dual Metal Sites for Efficient CO_2 to CO Electrolyzers at Industrial Current Densities

Manman Qi,[b,†] Michael J. Zachman,[c,†] Yingxin Li,[d,†] Yachao Zeng,[b,†] Sooyeon Hwang,[e] Jiashun Liang,[a] Mason Lyons,[f] Qian Zhao,[g] Yu Mao,[d] Yuyan Shao,[g] Zhenxing Feng,[f] Ziyun Wang,*[d] Yong Zhao,*[h] Gang Wu,*[a, b]

a. Department of Energy, Environmental, & Chemical Engineering, Washington University in St. Louis, St. Louis, MO 63130, United States. E-mail: gangw@wustl.edu

b. Department of Chemical and Biological Engineering University at Buffalo, The State University of New York, Buffalo, NY 14260, USA.

c. Centre for Nanophase Materials Sciences, Oak Ridge National Laboratory, Oak Ridge, TN 37831, USA.

d. School of Chemical Sciences, The University of Auckland, Auckland1010, New Zealand. E-mail: ziyun.wang@auckland.ac.nz

e. Centre for Functional Nanomaterials Brookhaven National Laboratory Upton, NY 11973, USA

f. School of Chemical, Biological, and Environmental Engineering Oregon State University, Corvallis, OR 97331, USA

g. Pacific Northwest National Laboratory, Washington 99354, United States

h. Commonwealth Scientific and Industrial Research Organization (CSIRO) Energy Centre, 10 Murray Dwyer Circuit, Mayfield West, NSW 2304, Australia. E-mail: y.zhao@csiro.au

† These authors contributed equally.
*Corresponding authors.

Experimental Section

Chemicals and reagents

All chemicals were of analytical grade and used without purification. Nickel (II) bis(acetylacetonate) (96%, acros organics), Fe_2O_3 nanoparticles with a size of ~5 nm (Alfa-Aesar), zinc nitrate hexahydrate (98%), methanol, ethanol, 2-methylimidazole (99%, Thermo Scientific), potassium bicarbonate (99.7% to 100.5 %, Thermo Scientific), Potassium chloride (99.0 to 100.5 %, Thermo Scientific), ultrapure water (Millipore, 18.2 MΩ cm). Nafion solution (5.0 wt.%), Nafion® 117 membrane, Nafion® 212 membrane, anion exchange membrane (Sustainion® 37-50, Dioxide Materials), gas diffusion layer (Sigracet, 22BC), and titanium foil were purchased from Fuel Cell Store. Ar and CO_2 (99.999%) were supplied by Air gas.

Catalyst preparation

Synthesis of CVD-Ni/Fe-N-C. Fe_2O_3@ZIF-8 was synthesized firstly according to our previous work.[1, 2] In a typical procedure, Fe_2O_3 nanoparticles with a size of ~5 nm (10 mg), and zinc nitrate hexahydrate (6.78 g) were dispersed and dissolved into a methanol solution (150 mL). The other methanol solution (150 mL) containing 2-methylimidazole (7.92 g) was prepared. Then, both solutions were mixed and heated at 60 °C for 24 hours. The resulting precipitant was collected and washed with ethanol three times, then dried at 60 °C in a vacuum oven to obtain the Fe_2O_3@ZIF-8 composite precursor. Take CVD-Ni_{82}/Fe_{14}-N-C catalyst as an example; 60 mg $Ni(acac)_2$ was placed upstream of a high-temperature alumina combustion boat, and 100 mg of Fe_2O_3@ZIF-8 precursors was set on the downstream side in a dual-zone tube furnace. The temperatures at the upstream (for $Ni(acac)_2$) and downstream (for Fe_2O_3@ZIF-8) in the dual-zone tube furnace were separately heated up to 240 and 400 ^{o}C at the same time under the argon atmosphere with a flow rate of 10 mL min^{-1}. Keep the temperature for two hours and increase the downstream temperature to 900 ^{o}C with a ramping rate of 10 ^{o}C min^{-1} to finish the carbonization process. The CVD-Ni/Fe-N-C samples were prepared by tuning the contents of $Ni(acac)_2$ with 4, 6.7, 20, and 100 mg. The carbonization temperatures were optimized from 800, 900, 1000 and 1100°C. Finally, the downstream carbonization duration varied from 1, 3, and 5 h to correlate the activity and product selectivity.

Synthesis of CVD-Ni-N-C. ZIF-8 was synthesized similarly to Fe_2O_3@ZIF-8 without Fe_2O_3 nanoparticles in a zinc nitrate hexahydrate methanol solution. The CVD-Ni-N-C catalyst was prepared by using a similar synthesis route as that for CVD-Ni/Fe-N-C, except for changing the Fe_2O_3@ZIF-8 to ZIF-8.

Synthesis of Fe-N-C and N-C. Fe-N-C and N-C samples were prepared by the same synthesis route as CVD-Ni/Fe-N-C by using Fe_2O_3@ZIF-8 precursors and ZIF-8 precursors, respectively, without $Ni(acac)_2$ at the upstream.

Physical characterization

Catalyst morphology and particle size were determined using a focused ion beam scanning electron microscope (FIB-SEM, CarlZeiss AURIGA CrossBeam) at a working voltage of 5 kV. The crystalline phases for different catalysts were identified using a powder X-ray diffraction (XRD, Rigaku Ultima IV diffractometer) with Cu Kα X-rays. X-ray fluorescence (XRF) was conducted on Malvern Panalytical Epsilon 1. The Raman spectra of catalysts coated on glass slides were determined using a Renishaw Raman system with an excitation laser of 514 nm and a constant excitation power of 150 μW. The catalyst surface area and porosity distribution were achieved using Brunnauer-Emmett-Teller (BET) and density functional theory (DFT) analyses of the N_2 isothermal adsorption/desorption measurement recorded at 77 K on a Micromeritics TriStar II with samples degassing at 150 ºC for 5 hours under vacuum. Thermo Scientific iCAP 6000 Inductively Coupled Plasma Optical Emission Spectrometer (ICP-OES) was applied to measure Fe, Ni, and Zn content in our studied catalysts. X-ray photoelectron spectroscopy (XPS) measurements were performed on a Physical Electronics Quantera Scanning X-ray Microprobe (Physical Electronics, Germany), which uses a focused monochromatic Al Kα (1486.7 eV) source for excitation. The X-ray beam is incident to normal to the sample, and the photoelectron detector is 45° off normal. High-energy resolution spectra were collected using a pass-energy of 69 eV with a step size of 0.125 eV. The wide scans were collected using a pass-energy of 140 eV with a step size of 0.5 eV. Thermogravimetric Analyzer (TGA) Instruments SDT Q600 were employed to analyze the samples under a nitrogen flow and heating rate of 10 ^{o}C min^{-1}.

Aberration-corrected HAADF-STEM images (**Fig. 4, S12, S14-15, S18-19**) and EELS point spectra (**Fig. S14-15**) for Fe-N-C, CVD-Ni-N-C, and CVD-Ni/Fe-N-C catalysts were acquired on a Nion UltraSTEM 100 operated at 60 kV with a ~31 mrad semiconvergence angle in the Center for Nanophase Materials Sciences (CNMS) at Oak Ridge National Laboratory (ORNL). Analysis of atom positions and nearest neighbor distances was performed using custom Python codes that track atom positions with sub-pixel accuracy[3]. Overall energy dispersive X-ray spectroscopic (EDS) quantification of the catalysts was performed on an aberration-corrected JEOL NEOARM operated at 80 kV in the CNMS at ORNL. In addition, HAADF-STEM and EELS maps were performed on an FEI Talos at Brookhaven National Laboratory (**Fig 1, S2, S16-17**). Ni and Fe K-edge X-ray absorption near edge structure (XANES) and extended X-ray absorption fine structure (EXAFS) measurements were carried out at Fe K-edge X-ray absorption spectroscopy was measured at beamline 11-2 of the Stanford Synchrotron Radiation Light (SSRL) source. Data was collected in fluorescence mode with Vortex detector. Raw data processed with Athena: background subtraction, normalization, and smooth background subtraction post-edge to minimize Fourier components below the first shell.[4] EXAFS fit using non-linear least squares fitting (Levenberg-Marquadt algorithm) for IFEFFIT ab initio calculations with Artemis GUI. Data used from k-space 2-12 A^{-1}.

CO_2RR experiments and MEA tests.

Electrode fabrication. To prepare the working electrode used in H-cell, 3.0 mg of catalyst was ultrasonically dispersed in 270 μL isopropanol and 30 μL Nafion solution (5 wt.%) to form homogeneous ink. Then, the catalyst ink was drop-casted onto a carbon paper-supported gas diffusion layer (effective area: 0.5 cm^2) and dried naturally to obtain a working electrode. For the MEA-based electrochemical measurement, the catalyst ink was sprayed onto the gas diffusion layer *via* airbrushing to form a catalyst layer with catalyst loading at 1 mg cm^{-2}. PTFE film-supported Ag substrates were used to test the CO_2RR performance in acidic conditions[5]. Then, the catalyst ink was sprayed onto the PTFE-Ag substrates to form the desired working electrodes.

Electrochemical measurements. Electrochemical measurements were conducted using electrochemical workstations CHI 630 and Autolab PGSTAT302N connected to a current booster (Metrohm Autolab, 10 A). A gas-tight H-type cell separated by a Nafion® 117 membrane coupled with a working electrode and a reference electrode (Ag/AgCl, 3 M KCl) in the cathode chamber and a counter electrode (1 × 1 cm Pt foil) in the anode chamber. The electrocatalytic performance of samples was tested in CO_2 (99.999%)-saturated 0.5 M $KHCO_3$ with the volume at 40 mL in each chamber. A continuous stream of CO_2 at a flow rate of 30 mL/min is introduced to the cathodic chamber along with stirring the catholyte during the test. Cyclic voltammetry is repeatedly performed until the cathodic currents are stable. Then a linear sweep voltammetry with a scan rate at 5 mV s^{-1} was conducted with 90% *iR* compensation. Then, a chronoamperometric measurement with 90% *iR* compensation was performed for continued electrolysis at each potential for about 12 min. The measured potentials are rescaled to the reversible hydrogen electrode by E (*vs*. RHE) = E (*vs*. Ag/AgCl) + 0.197 V + 0.0591 V × pH.

We assembled a CO_2RR working electrode with a titanium mesh-supported IrO_x anode and an anion exchange membrane (Sustainion® 37-50, Dioxide Materials) to test the CO_2RR performance in a membrane electrode assembly (MEA) electrolyzer. Reaction gas CO_2 was fed to the cathode at a flow rate of 20 mL/min, and 0.1 M $KHCO_3$ was used as an electrolyte to circulate in the anode chamber with a flow rate of 5 mL/min. The acid flow cell was tested in a slim flow cell, using a Pt mesh as an anode, 0.5 M H_2SO_4 as anolyte, 0.025 M H_2SO_4 and 3 M KCl solution as catholyte, and Nafion® 212 as the separator. The MEA and flow cell tests were conducted without iR compensation at each current density.

Qualification of CO and H_2. The products were determined using similar procedures as previous works.[6] The products are analyzed via an online gas chromatograph (GC, Agilent 7890B) equipped with two HP-Plot Q Capillary Columns and an HP-Plot Molesieve (Agilent) column. The thermal conductivity detector (TCD) was used to detect the generated H_2, and a methanizer-assisted flame ionization detector (FID) was employed to detect CO and CH_4. Although the liquid product was not analyzed using H-NMR in this work, it is known from our previous work[7, 8] and reported literature[9-11] that atomically-dispersed M-N-C catalysts for CO_2RR only led to the production of CO and H_2. The near-unity value of FE was also confirmed.

Faradaic efficiency (FE) calculation. The FE can be written as:

$$FE = \frac{Q_{gas}}{Q_{total}} \times 100\% = \frac{(\frac{v}{60s/min}) \times (\frac{x}{V_m}) \times N \times F}{I}$$

Where, v: volumetric flow rate (20 ml min^{-1}); x is the measured concentration of gas product in sample loop referring to standard curve (part per million, ppm); is the measured concentration of gas product in sample loop referring to standard curve (part per million, ppm); V_m is the gaseous molar volume (24000 mL mol^{-1} at 25 °C, 101 kPa); N: the number of electrons transferred during the reaction (here is 2); F: Faradaic constant (96485 C mol^{-1}); I: total current (A).

Turnover frequency (TOF h^{-1}) of CO. TOFs for production were evaluated based on the two electrons pathway:

$$TOF = \frac{\frac{I_{CO}}{N \times F}}{m_{cat} \times \frac{w}{M_{metal}}} \times 3600$$

Where I_{CO} is the partial current (A) of CO formation; N (here is 2) is the transferred electrons numbers for one molecule product; F is the Faradaic constant, 96485 C mol^{-1}; m_{cat} is the catalyst mass (*g*) on the electrode; ω is the mass fraction (wt.%) of metal obtained from the XPS analysis; M_{metal} is the atomic mass of Ni (58.69 g mol^{-1}) or Fe (55.85 g mol^{-1}).

Electrochemical active surface areas (ECSA) measurements. The ECSA is proportional to double-layer capacitance (C_{dl}) values. C_{dl} was determined in a rotating disk electrode (RDE) with catalysts loading at 0.2 mg cm^{-2}. The capacitive current associated with the double layer was recorded by changing the scan rate of cyclic voltammetry (CV). The potential of CV ranged from −0.10 to −0.20 V *vs*. RHE, and the scan rates were 5, 10, 20, 30, 40 and 50 mV s^{-1}. The double-layer capacitance is estimated by plotting the Δj calculated by $(j_a\text{-}j_c)/2$ at −0.15 V *vs*. RHE against the scan rate. The equation calculated ECSA: ECSA= $C_{dl}/21\mu\mathrm{F\ cm}^{-2}$.

DFT calculations

All calculations were carried out with the Perdew-Burke-Ernzerhof (PBE)[12] functional using Vienna ab initio simulation package (VASP).[13, 14] The implicit solvent effect is considered through the solvation model based on the VASPsol.[15, 16] The dielectric constant of liquid water is set to be 80. The project-augmented wave (PAW) method represented the core–valence interaction.[17, 18] For total energy calculations, a cut-off energy of 450 eV was set for plane wave basis sets to expand the valence electronic states. Spin polarization was included in all calculations to describe magnetic systems accurately. The Beck-Johnson damping correction method[19] included van der Waals (vdW) interactions. To properly describe the iron atom, the DFT+U method is applied where the on-site coulomb correction was set on Fe and Ni *3d* orbitals with effective U-J values of 3.29 and 3.40 eV, respectively, as suggested in other theoretical works.[20, 21] The Brillouin zone was sampled 2×2×1, and a vacuum layer of 15 Å was applied to avoid lateral interactions. All atoms were fully relaxed until the force on each atom was lower than 0.05 eV/Å. All models are shown in **Figure S26**.

For hydrogen evolution reaction (HER), we consider the adsorption of free energy of H* as the HER activity descriptor ($H^+ + e^- + * \rightarrow H^*$). For CO_2RR to CO, the following three elementary reactions are considered:

$$CO_2\,(g) + H^+ + e^- + * \rightarrow COOH^*$$

$$COOH^* + H^+ + e^- \rightarrow CO^* + H_2O$$

$$CO^* \rightarrow CO\,(g) + *$$

The Gibbs free energy differences of these intermediates include zero-point energy (ZPE), thermal energy, and entropy derived from partition functions.[22, 23] The ZPE correction is given by:

$$E_{ZPE} = \sum_i \frac{hv_i}{2}$$

where h is Plank's constant and v_i is vibrational frequency i, which is calculated based on the harmonic oscillator approximation. The standard molar vibrational thermal energy contribution is calculated by:

$$U_{vib} = RT\sum_i \frac{hv_i/k_B}{e^{hv_i/k_BT} - 1}$$

where R is the gas constant and k_B is Boltzmann's constant. The standard molar vibrational entropy is calculated using the following expression:

$$S_{vib} = R\sum_i [\frac{hv_i/k_BT}{e^{hv_i/k_BT} - 1} - \ln(1 - e^{hv_i/k_BT})]$$

Therefore, the standard molar Gibbs free energies are obtained by:

$$G = E_{total} + E_{ZPE} + U - TS$$

where E_{total} refers to the total energy obtained from DFT calculations. The solvation effect correction was 0.25 eV stabilization of *COOH and 0.1 eV stabilization of *CO.[24, 25]

Additional Figures

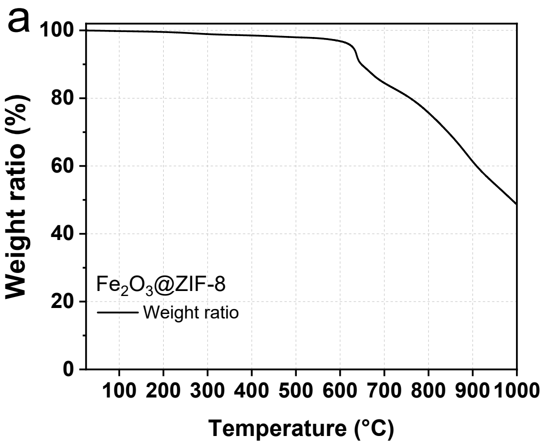

Figure S1. TGA of (a) Fe_2O_3@ZIF-8 and (b) Ni(acac)$_2$ power under nitrogen with a heating rate of 10 ^{o}C min^{-1}. Fe_2O_3@ZIF-8 precursor was stable before 600 ^{o}C. Ni(acac)$_2$ started decomposing at ~250 ^{o}C and completed at around 470 ^{o}C.

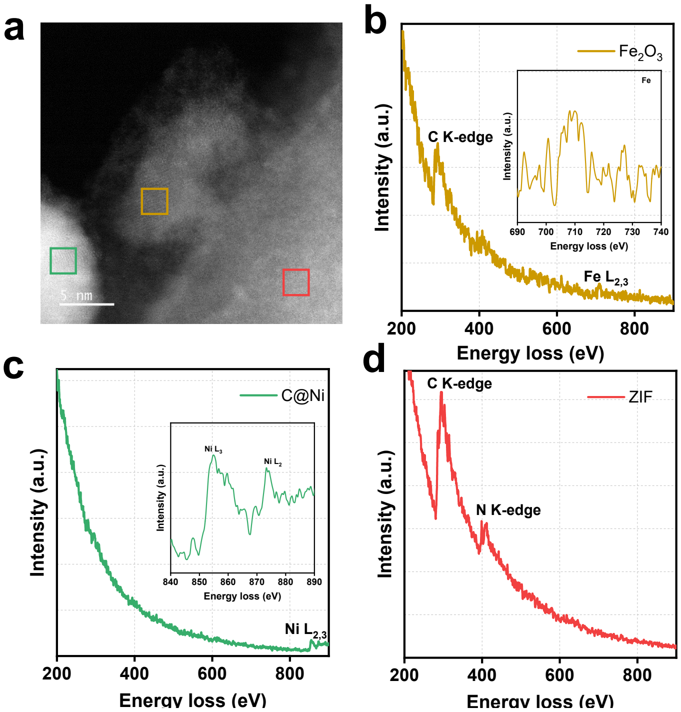

Figure S2. (a) HAADF-STEM image of CVD intermediate with C@Ni nanoparticles and Fe_2O_3@ZIF-8. (b-d) EELS spectra of the intermediate at three rectangular regions representing Fe-L-edge (b), ZIF body (c), and Ni-L-edge(d), respectively.

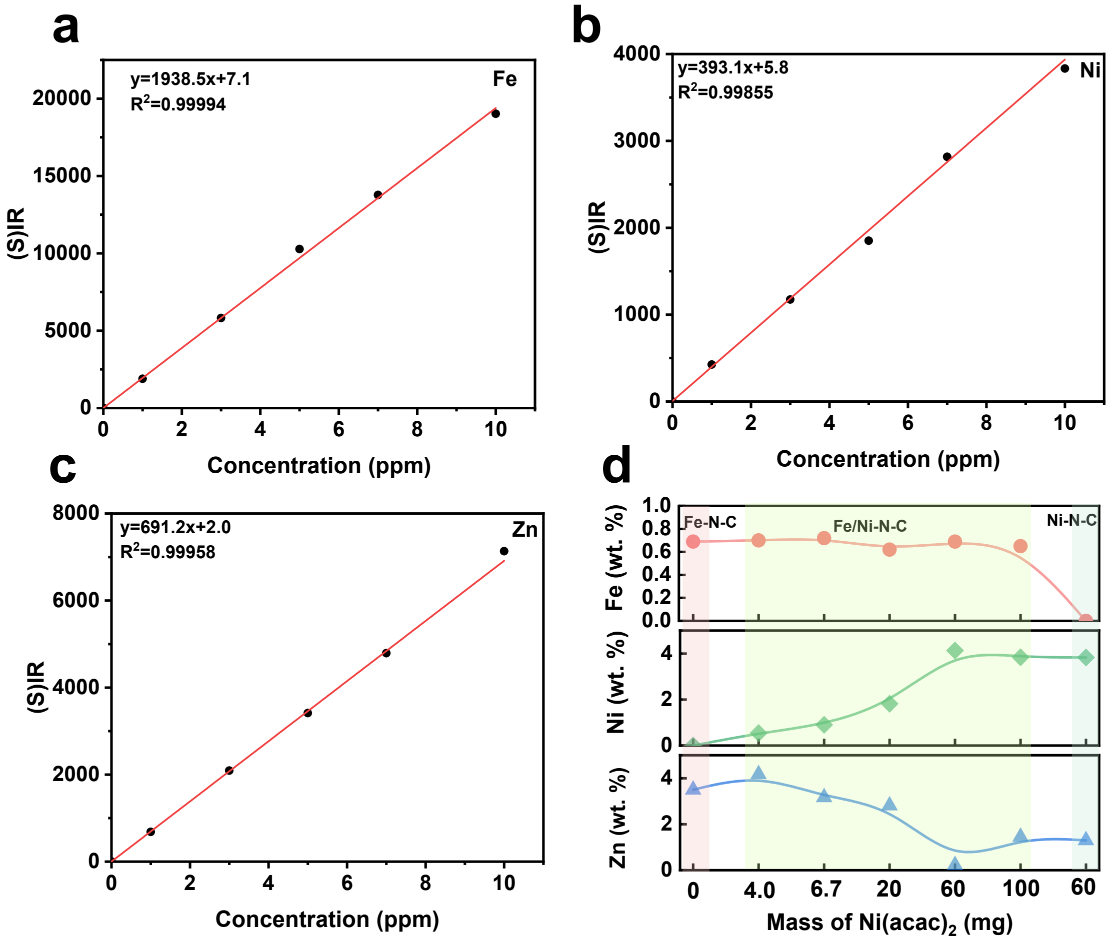

Figure S3. (a-c) ICP-OES determination of Fe (a), Ni (b), and Zn (c) contents by using the standard calibration solutions, ranging from 0 to 10 ppm. (d) The metal loadings of Fe-N-C and CVD method prepared Ni/Fe-N-C and Ni-N-C catalysts.

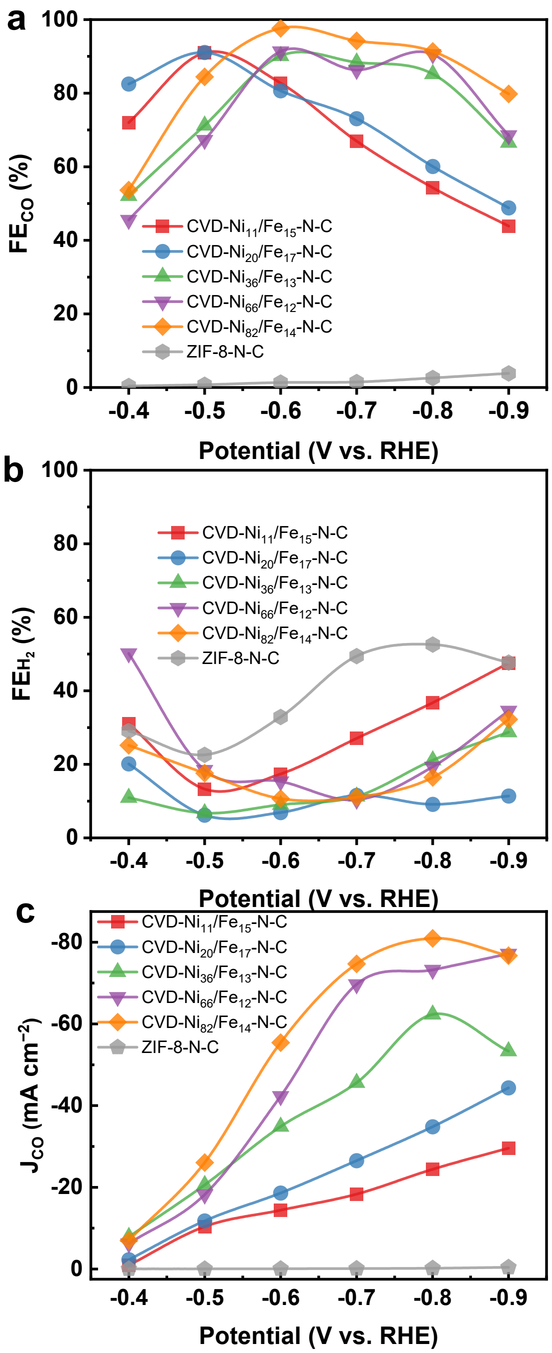

Figure S4. Electrocatalytic CO_2 reduction performance in H-cell with CO_2-saturated 0.5 M $KHCO_3$ as electrolyte. FEs of (a) CO (b) H_2 (c) J_{CO} for ZIF-8-N-C, CVD-Ni_{11}/Fe_{15}-N-C, CVD-Ni_{20}/Fe_{17}-N-C, CVD-Ni_{36}/Fe_{13}-N-C, CVD-Ni_{66}/Fe_{12}-N-C, CVD-Ni_{82}/Fe_{14}-N-C catalysts. These numbers under subscription are the molar ratios of Ni and Fe, which were determined by the ICP-OES analyses.

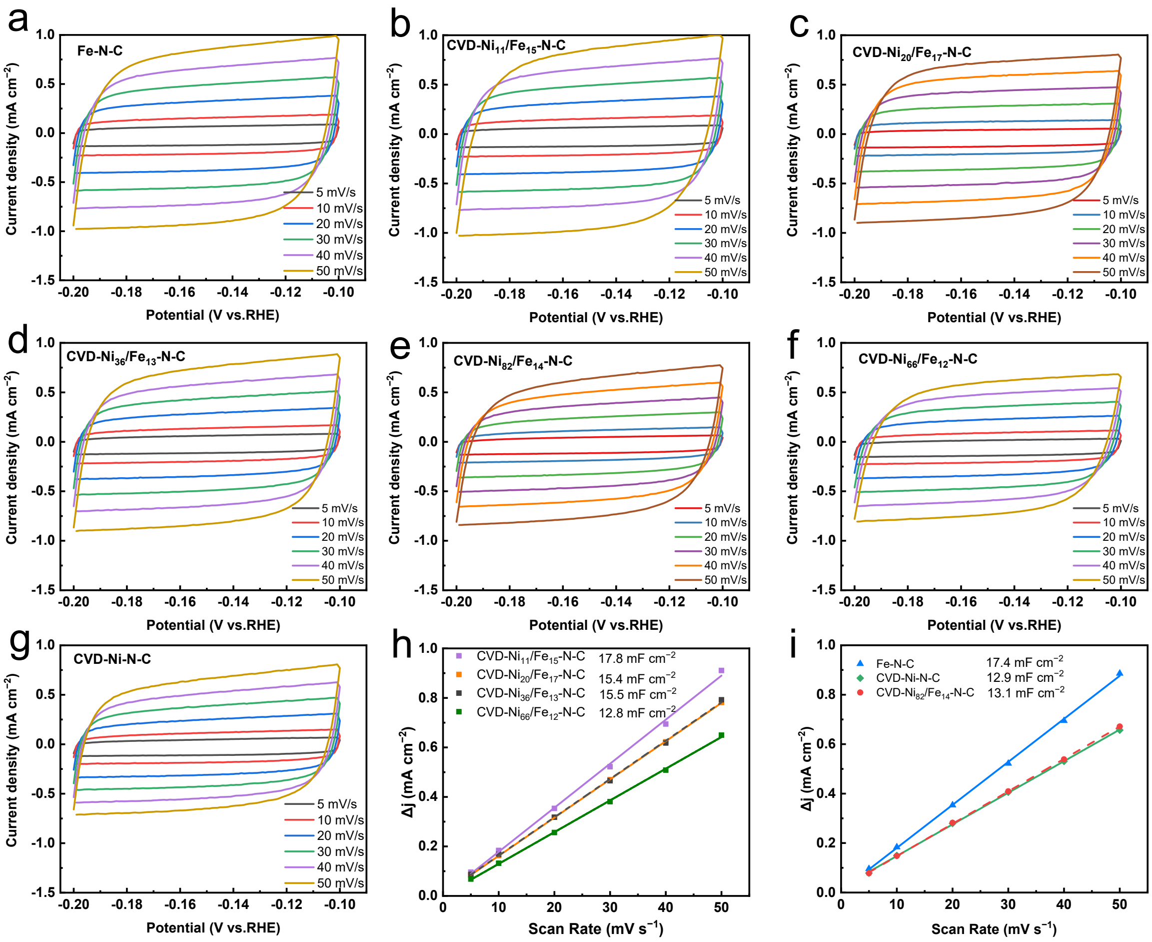

Figure S5. Cyclic voltammetry curves from −0.10 to −0.20 V vs. RHE at scan rates ranging from 5 to 50 mV s^{-1} for (a) Fe-N-C, (b) CVD-Ni_{11}/Fe_{15}-N-C, (c) CVD-Ni_{20}/Fe_{17}-N-C, (d) CVD-Ni_{36}/Fe_{13}-N-C, (e) CVD-Ni_{82}/Fe_{14}-N-C, (f) CVD-Ni_{66}/Fe_{12}-N-C, (h) CVD-Ni-N-C. (h-i) The plot of charging current density differences Δ*j* against the scan rate.

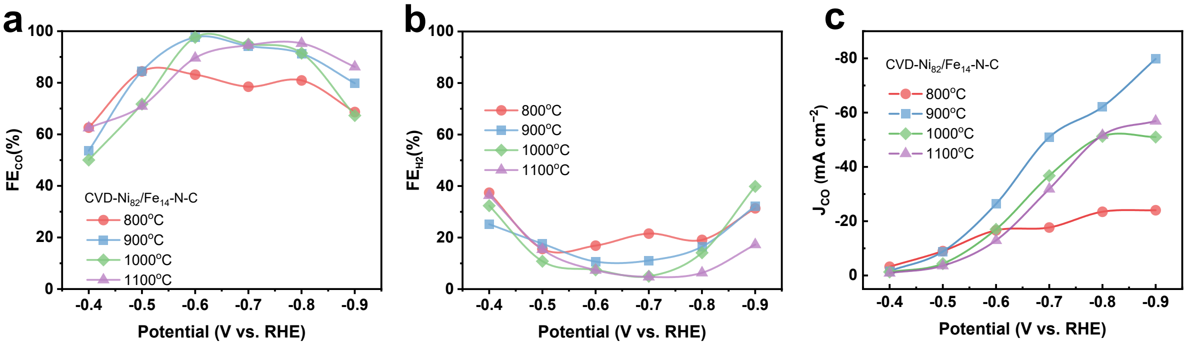

Figure S6. FEs of (a) CO (b) H_2 (c) J_{CO} for CVD-Ni_{82}/Fe_{14}-N-C catalysts with different heat-treatment temperatures for one hour.

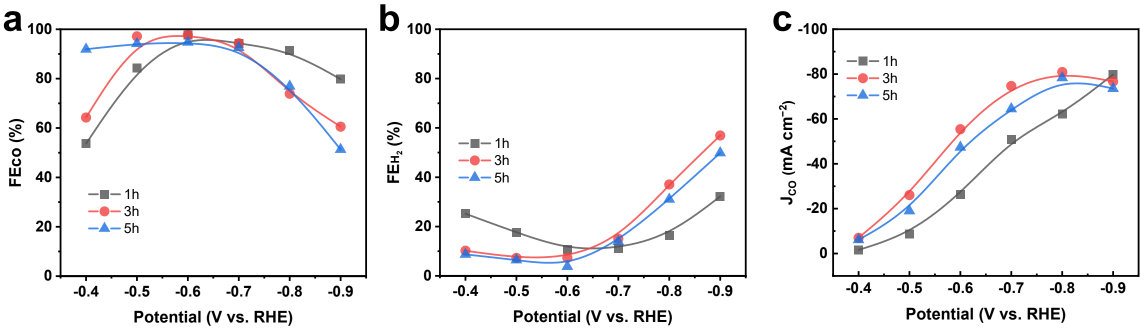

Figure S7. FEs of (a) CO (b) H_2 (c) J_{CO} for CVD-Ni_{82}/Fe_{14}-N-C catalysts with different heat-treatment times at 900 °C.

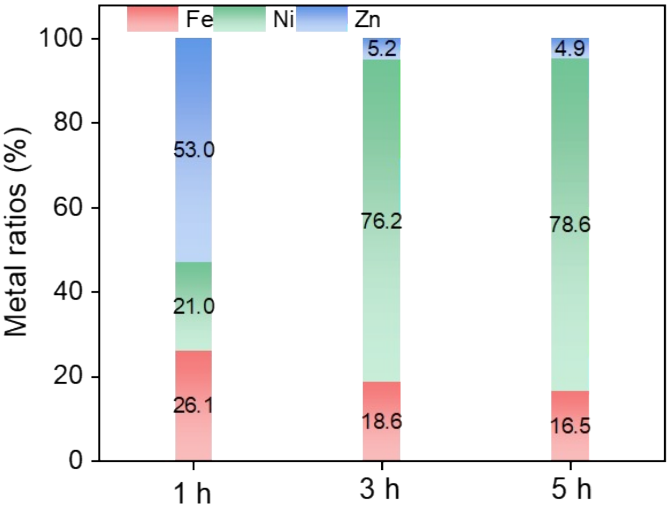

Figure S8. XRF results of CVD-Ni/Fe-N-C heat treated at 900 °C for one, three, and five hours.

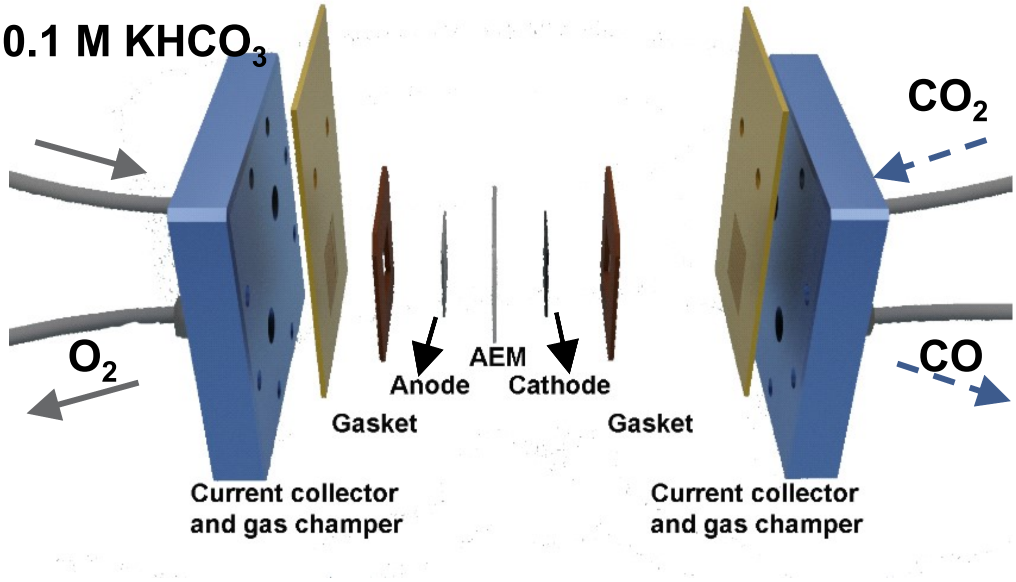

Figure S9. A schematic illustration of a zero-gap MEA with 0.1 M $KHCO_3$ as the electrolyte.

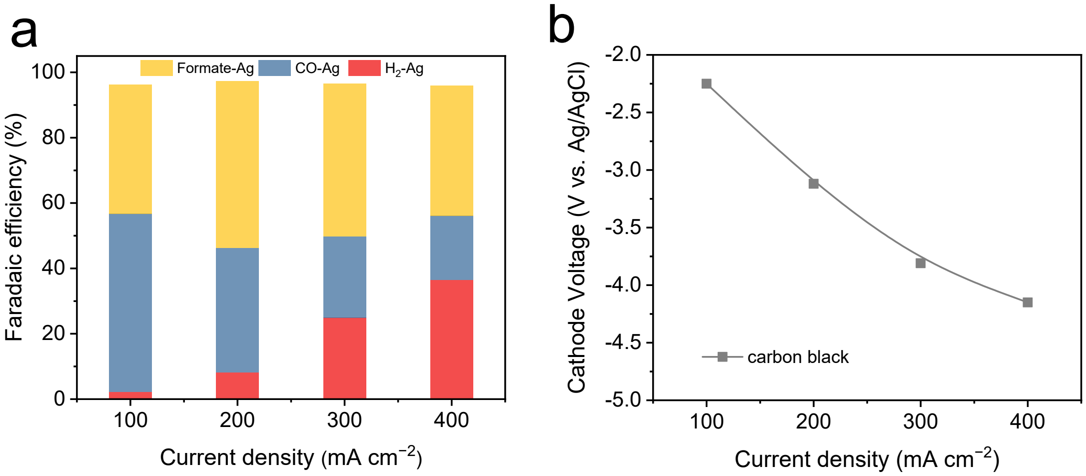

Figure S10. (a) FEs of formate, CO, and H_2 (b) cathode potential vs. Ag/AgCl of carbon black on ePTFE-Ag substrate in an acid flow cell.

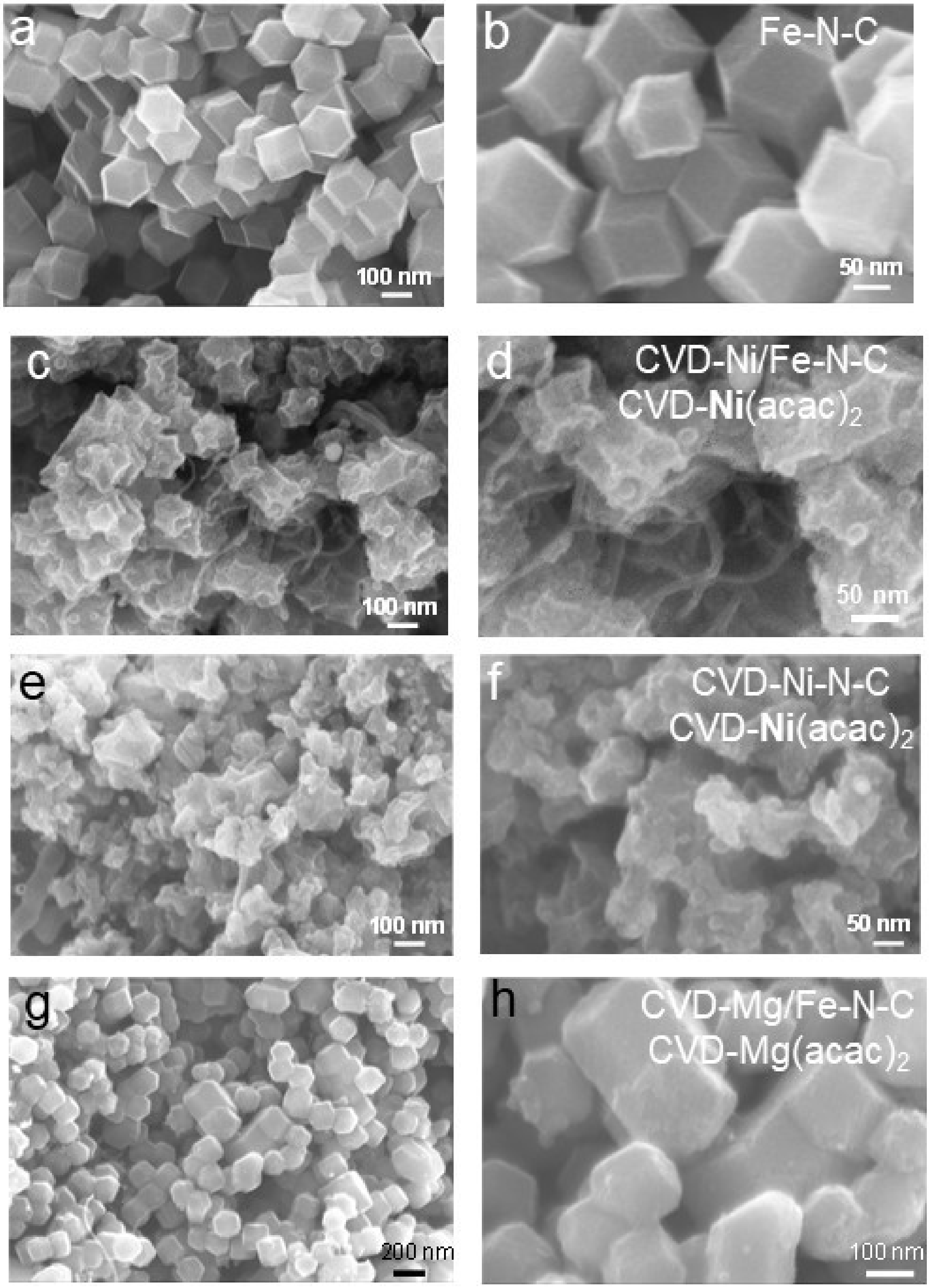

Figure S11. SEM images at different magnifications of (a-b) Fe-N-C, (c-d) CVD-Ni/Fe-N-C, (e-f) CVD-Ni-N-C, and (g-h) CVD-Mg/Fe-N-C samples.

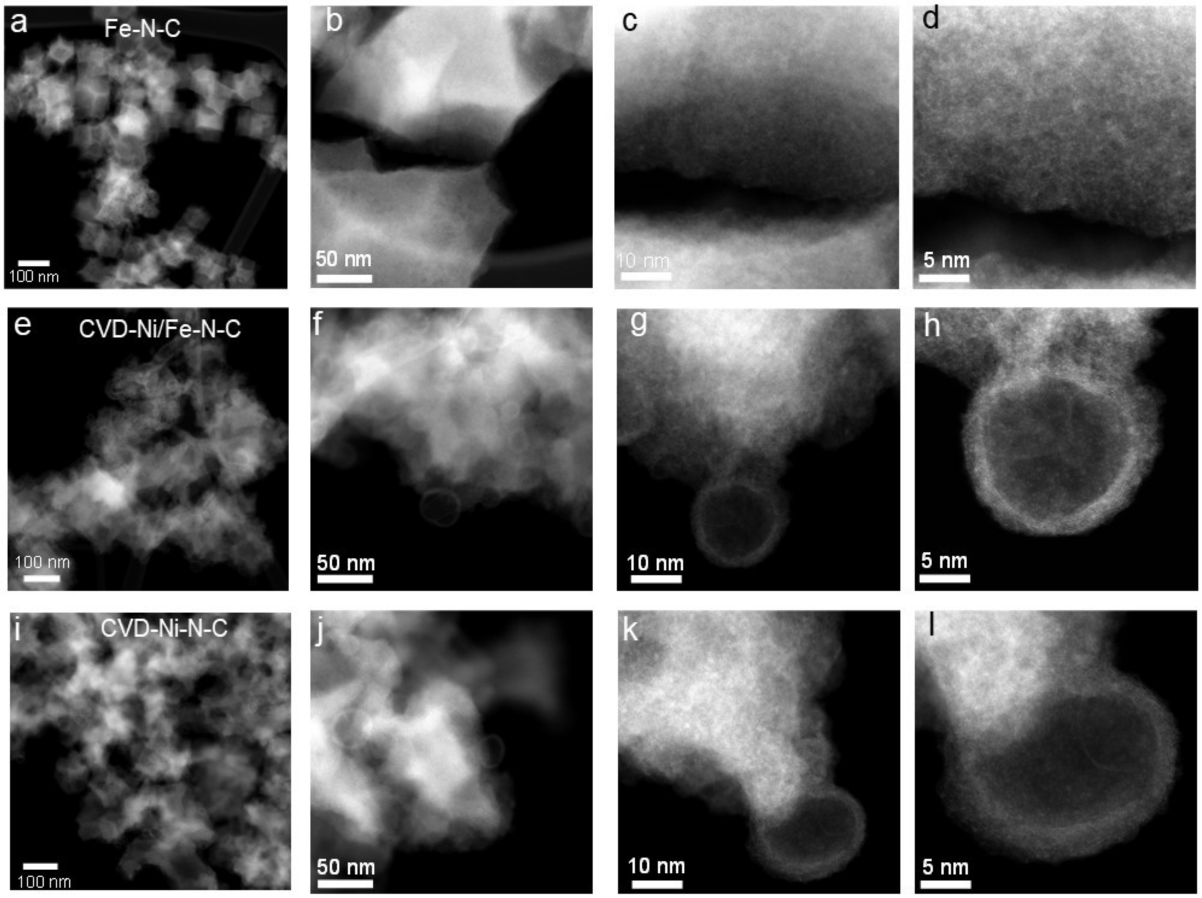

Figure S12. HAADF-STEM images at different scales of (a-d) Fe-N-C, (e-h) CVD-Ni/Fe-N-C, (i-l) CVD-Ni-N-C.

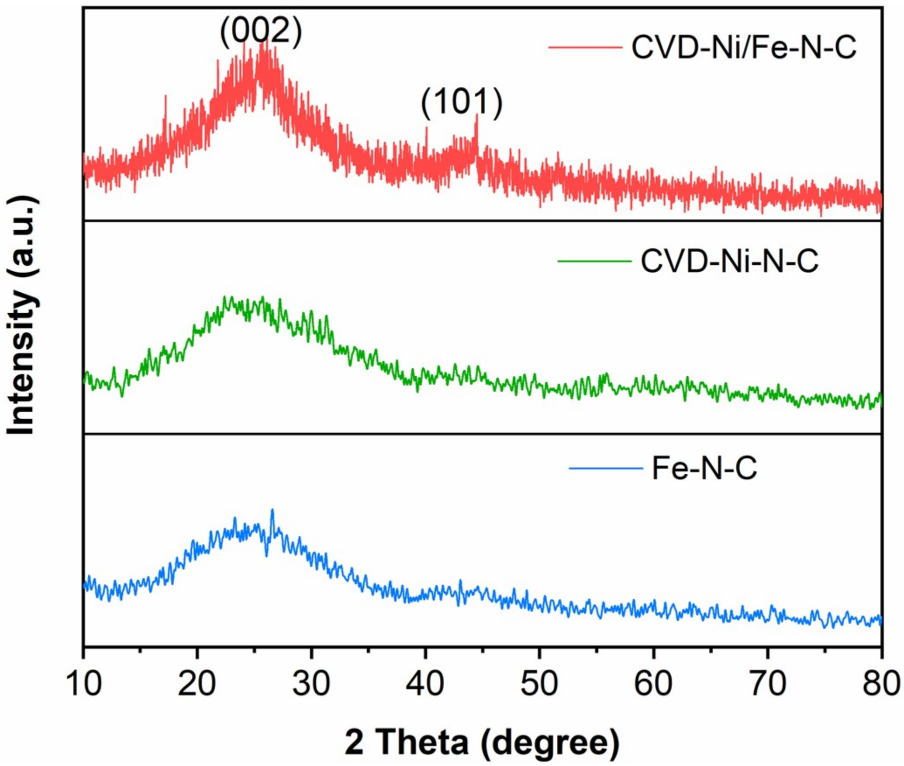

Figure S13. XRD patterns of Fe-N-C, CVD-Ni-N-C, and CVD-Ni/Fe-N-C.

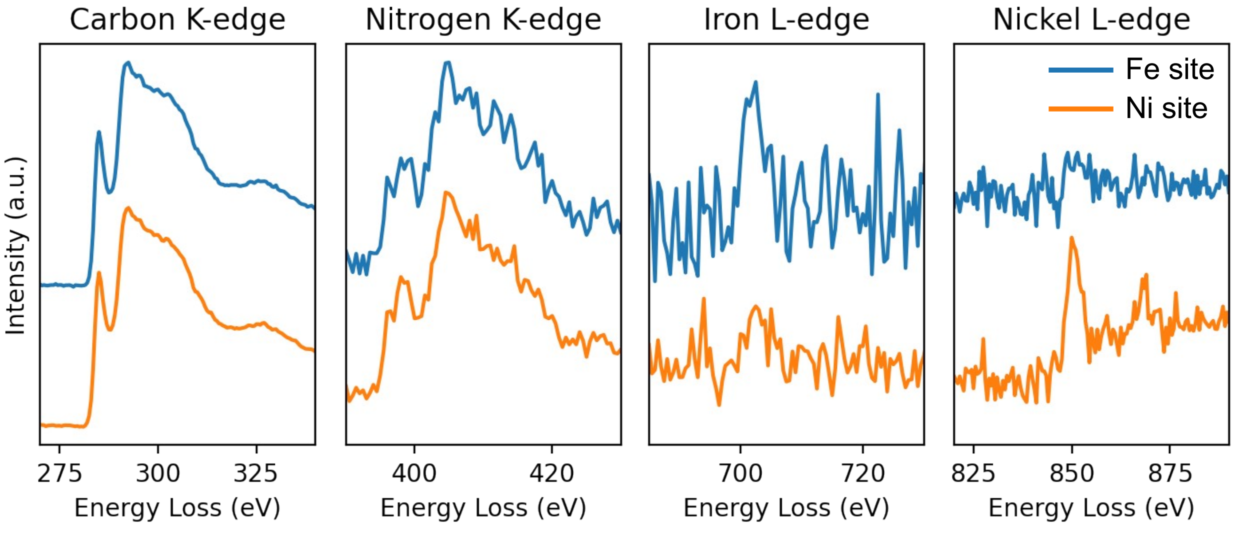

Figure S14. Average EELS point spectra of CVD-Ni/Fe-N-C catalyst (402 eV for N-K, 708/721 eV for Fe-$L_{2,3}$, and 855/872 eV for Ni-$L_{2,3}$ edges).

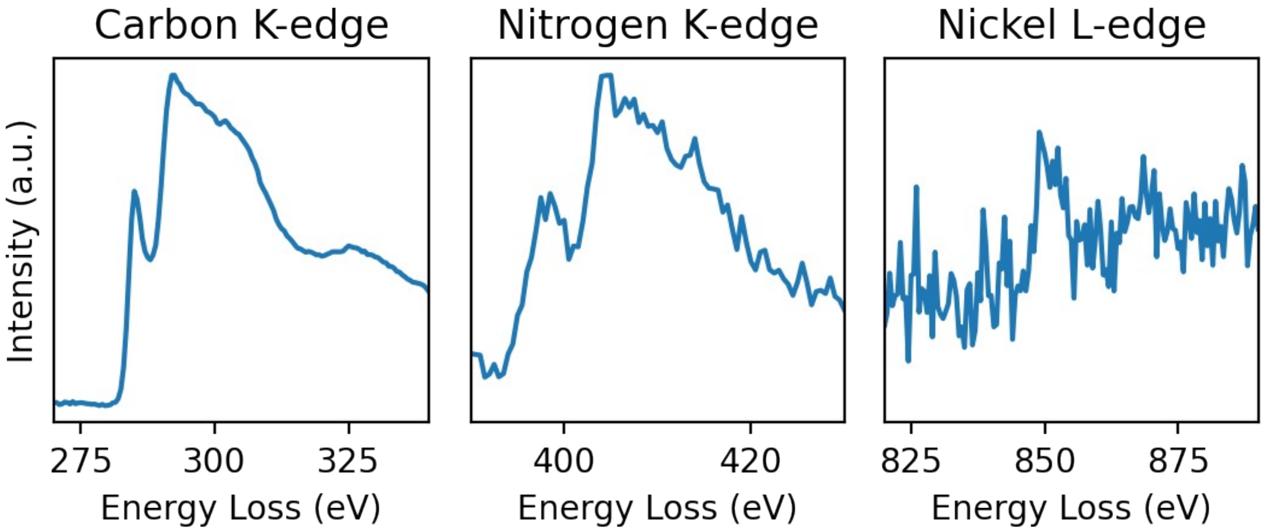

Figure S15. Average EELS point spectra of CVD-Ni-N-C catalyst (402 eV for N-K, and 855/872 eV for Ni-$L_{2,3}$ edges).

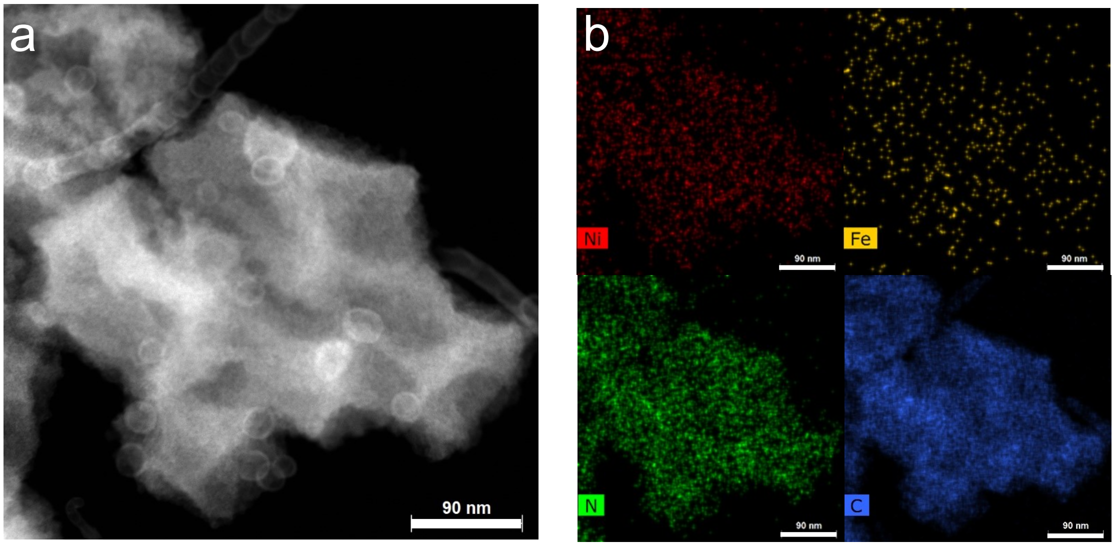

Figure S16. (a) HAADF-STEM image of CVD-Ni/Fe-N-C and corresponding elemental mappings (b) of Ni, Fe, N, and C.

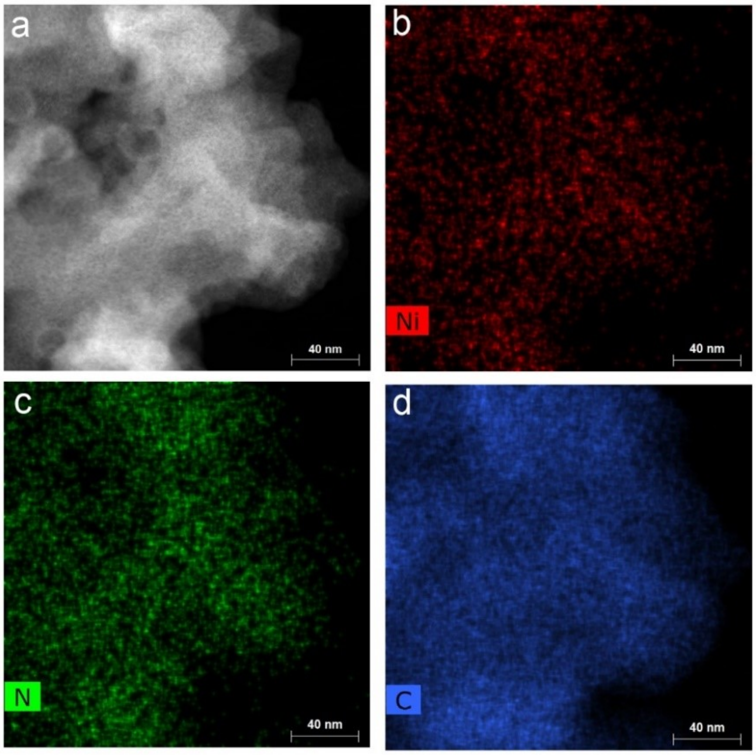

Figure S17. (a) HAADF-STEM image of CVD-Ni-N-C and the corresponding elemental mappings of Ni (b), N (c), and C (d).

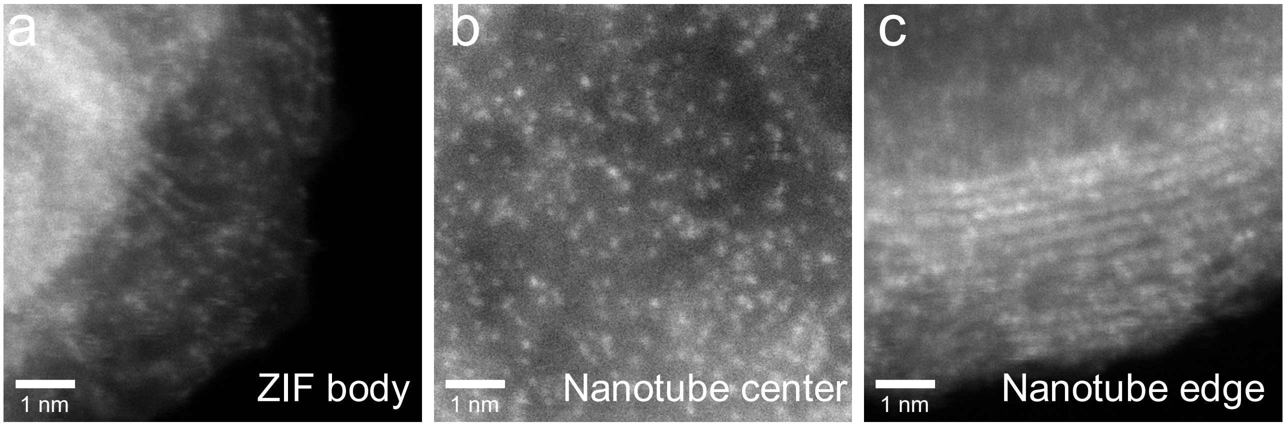

Figure S18. HAADF-STEM images of CVD-Ni-N-C at three typical areas, i.e., ZIF body (a), nanotube center (b), and nanotube edge (c).

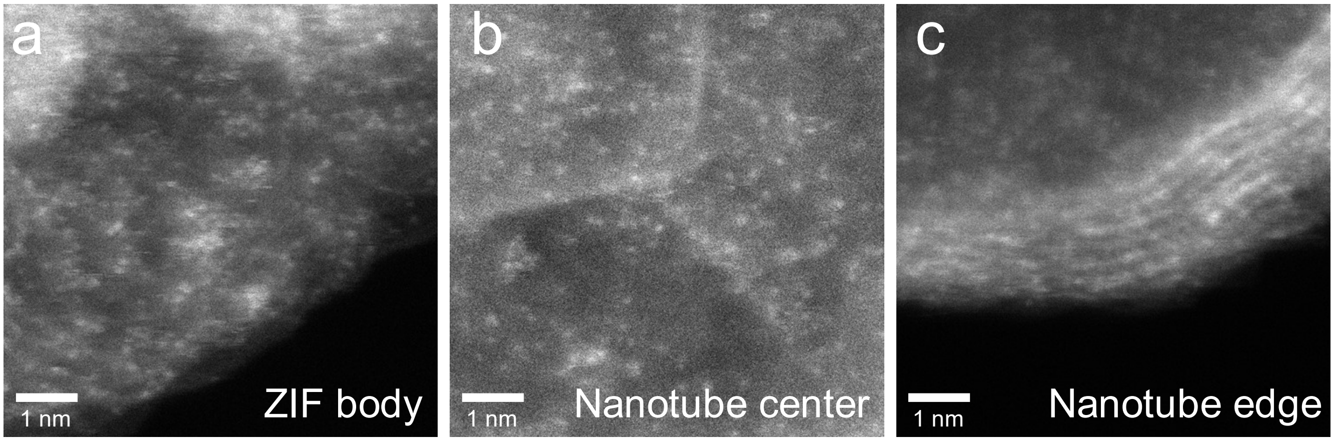

Figure S19. HAADF-STEM images of CVD-Ni/Fe-N-C at three typical areas, i.e., ZIF body (a), nanotube center (b), and nanotube edge (c).

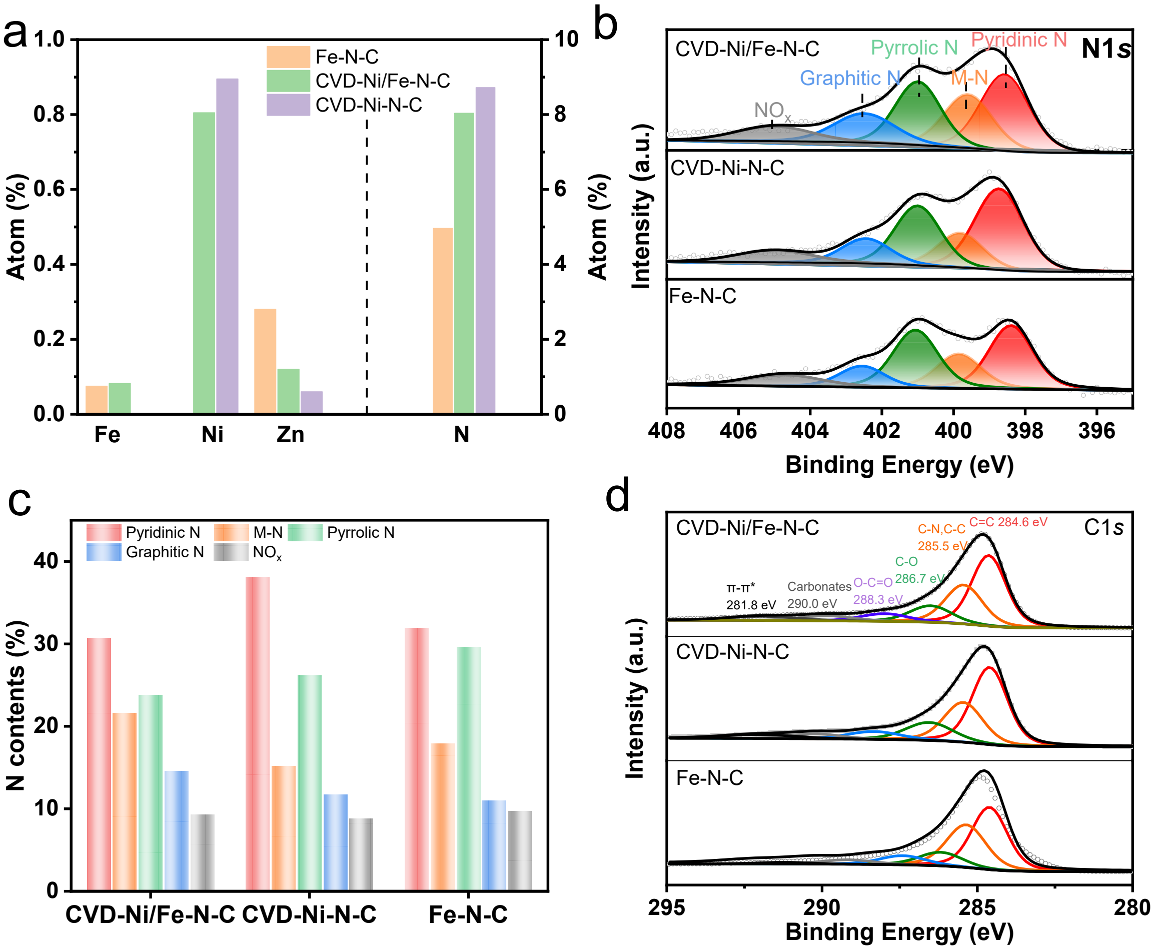

Figure S20. (a) Elemental contents of Fe, Ni, Zn, and N were obtained from XPS. (b) High-resolution XPS N 1s spectra of prepared samples. (c) Nitrogen contents of samples derived from N 1s peak fittings. (d) High resolution of C 1s spectrum of CVD-Ni/Fe-N-C, Ni-N-C, and Fe-N-C catalysts.

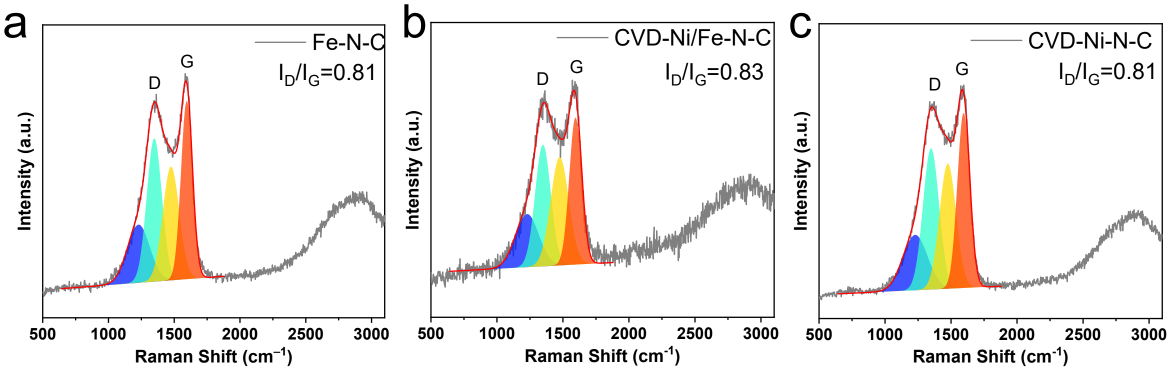

Figure S21. Raman spectroscopy of (a) Fe-N-C, (b) CVD-Ni/Fe-N-C, and (c) CVD-Ni-N-C catalysts.

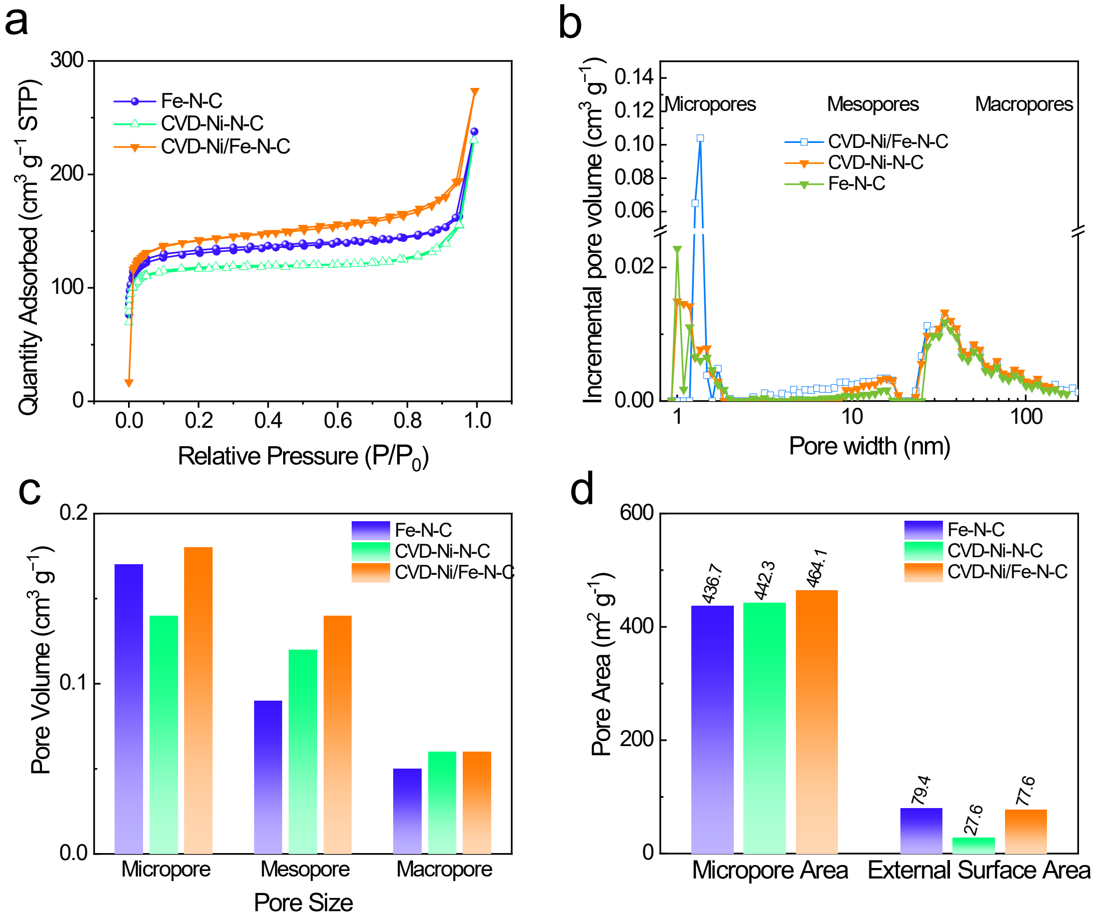

Figure S22. (a) N_2 sorption isotherm at 77 K, (b) pore size distribution calculated by the DFT model BET, (c) pore volume, and (d) pore area of Fe-N-C, CVD-Ni-N-Cand CVD-Ni/Fe-N-C catalysts.

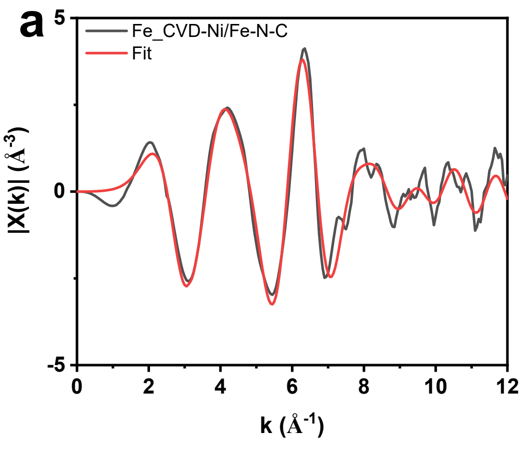

Figure S23. The k-space EXAFS curve of CVD-Ni/Fe-N-C at Fe K-edge (a) and Ni K-edge(b).

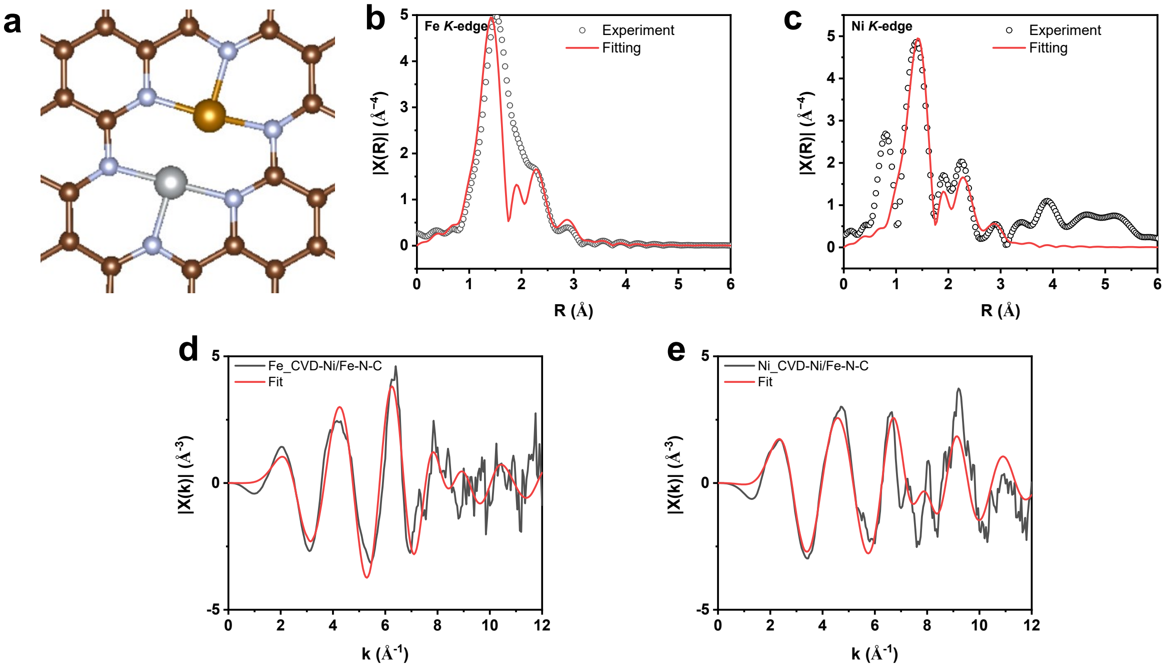

Figure S24. (a) Fitting model of Non-bridged (0-N) for CVD-Ni/Fe-N-C. The brown, light grey, grey, and dark brown balls represent C, N, Ni and Fe atoms, respectively. The R-space EXAFS-fitting curves of the CVD-Ni/Fe-N-C at Fe K-edge (b) and Ni K-edge (c). The k-space EXAFS curve at Fe K-edge (d) and Ni K-edge(e).

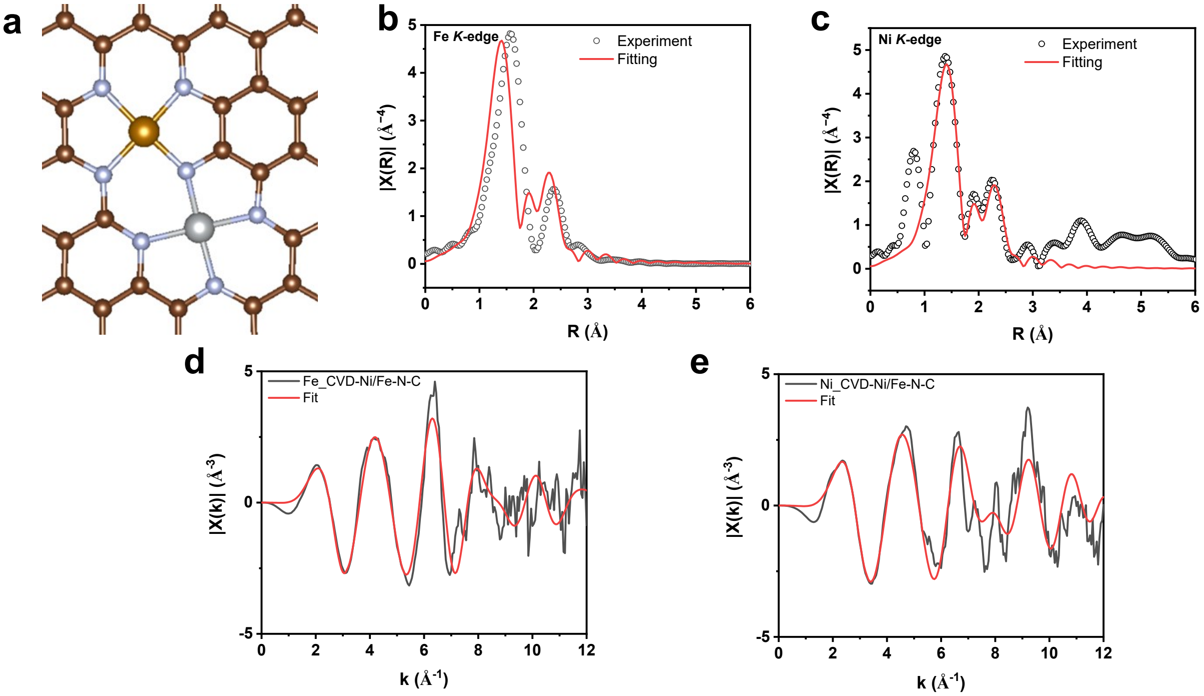

Figure S25. (a) Fitting model of single-bridged (1-N) for CVD-Ni/Fe-N-C. The brown, light grey, grey, and dark brown balls represent C, N, Ni, and Fe atoms, respectively. The R-space EXAFS-fitting curves of the CVD-Ni/Fe-N-C at Fe K-edge (b) and Ni K-edge (c). The k-space EXAFS curve at Fe K-edge (d) and Ni K-edge(e).

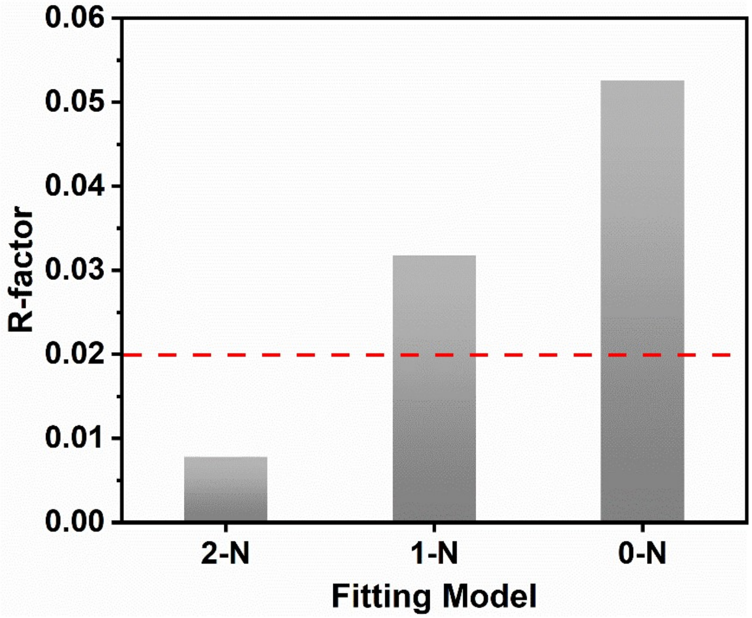

Figure S26. R factors of the fitting models of Double-bridged (2-N), single-bridged (1-N), and Non-bridged (0-N). R-factor below 2% is generally considered acceptable.

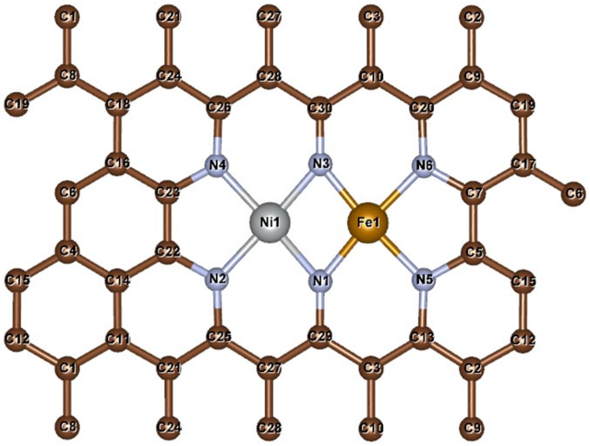

Figure S27. Configuration of CVD-Ni/Fe-N-C dual atom site derived from **Table S10** with the coordinated atoms labeled.

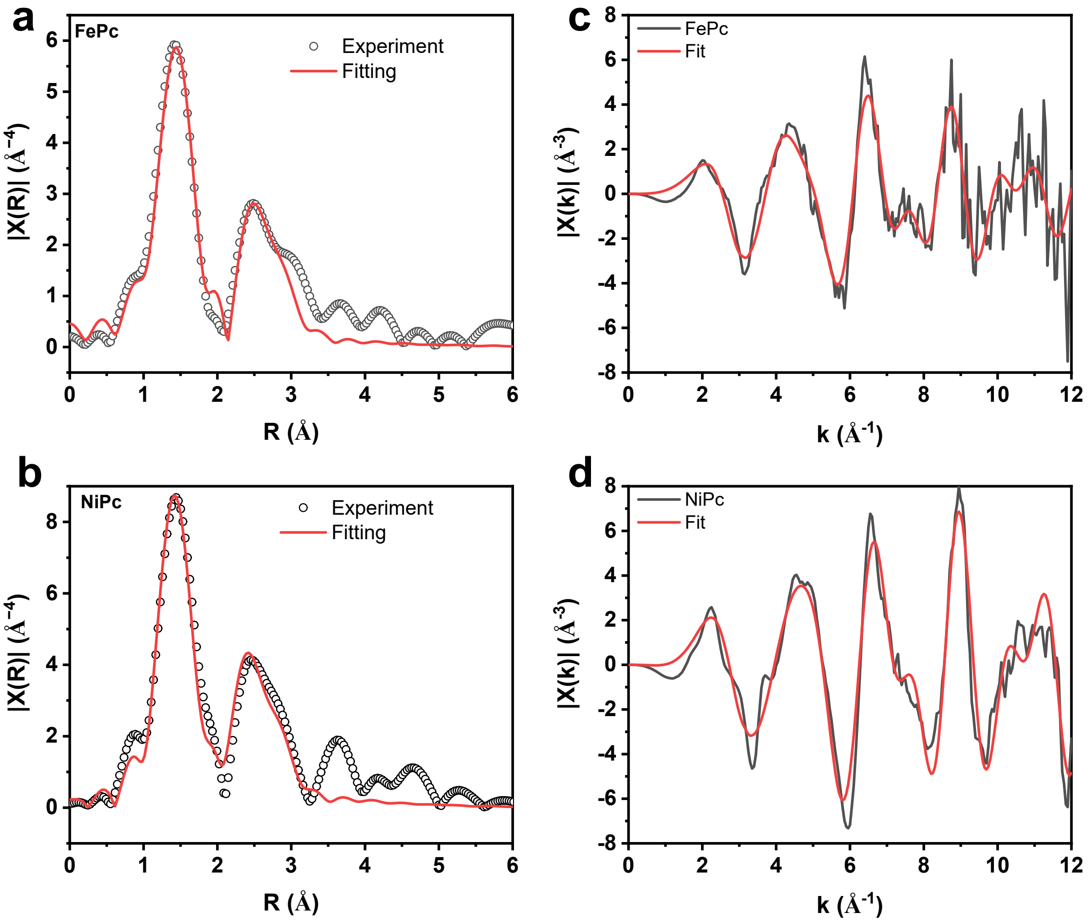

Figure S28. (a-b) The R-space EXAFS-fitting curves of the FePc (a) and NiPc (c). (c-d) The k-space EXAFS curve of FePc (c) and NiPc (d).

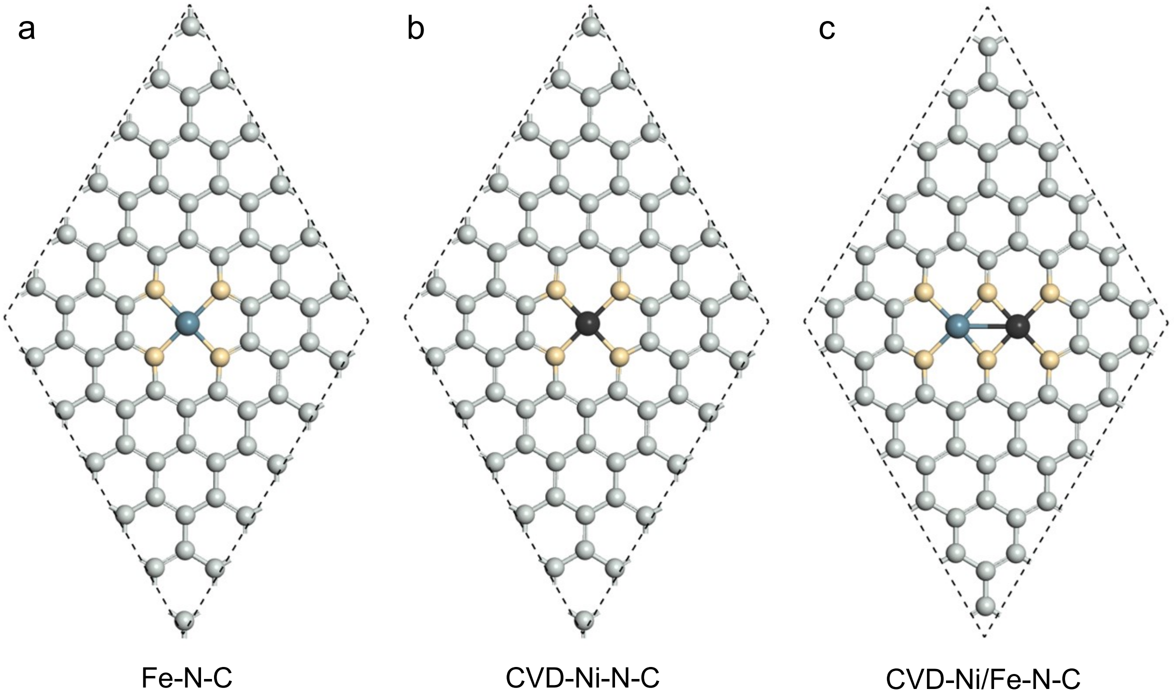

Figure S29. Optimized geometric structures of Fe-N-C (a), Ni-N-C (b), and CVD-Ni/Fe-N-C (c) surfaces, where C atoms in light gray, N atoms in beige, Fe in blue, and Ni in black.

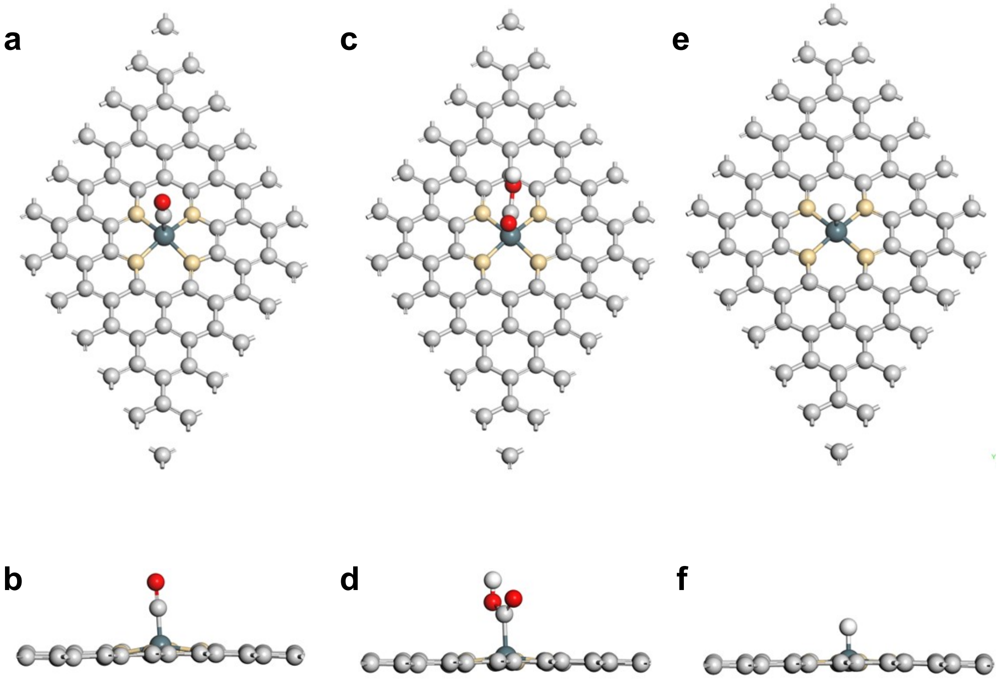

Figure S30. Optimized geometric structures of Fe-N-C with *CO (a-b), *COOH (c-d), *H (e-f) attached, where C atoms in light gray, N atoms in beige, O in red, H in white, and Fe in blue.

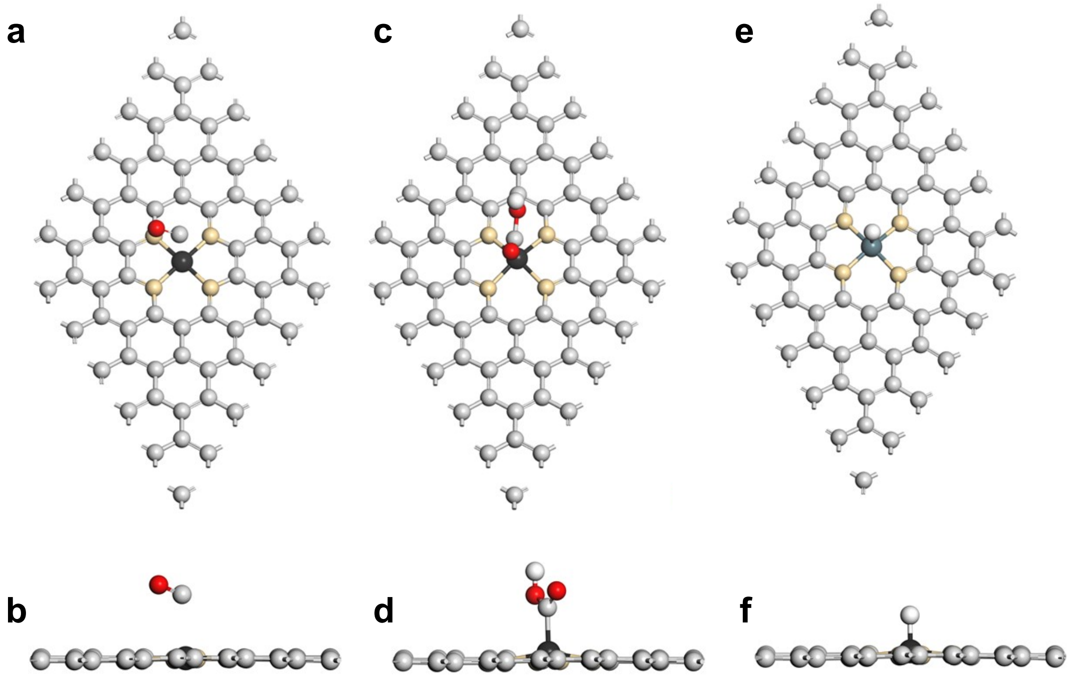

Figure S31. Optimized geometric structures of CVD-Ni-N-C with *CO (a-b), *COOH (c-d), *H (e-f) attached, where C atoms in light gray, N atoms in beige, O in red, H in white, and Ni in black.

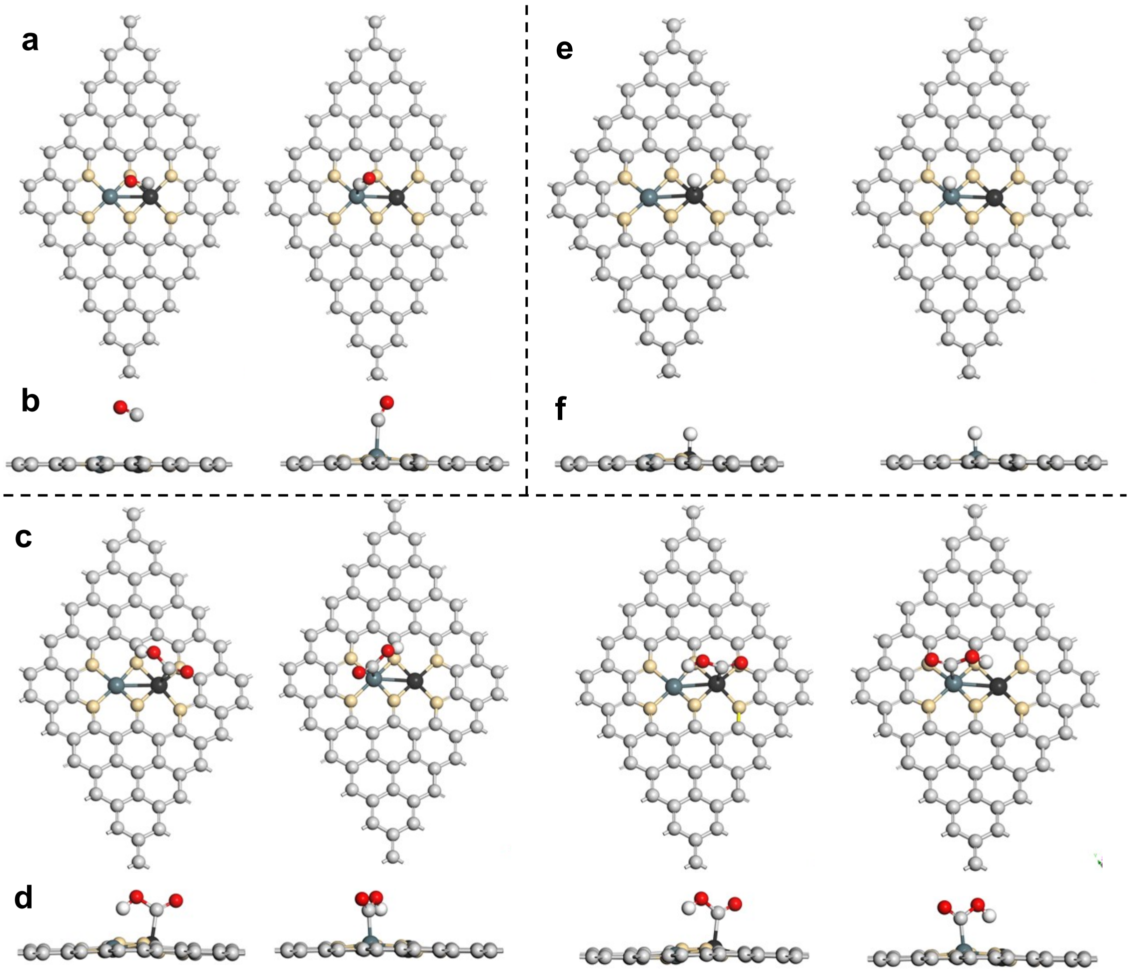

Figure S32. Optimized geometric structures of possible CVD-Fe/Ni-N-C with *CO (a-b), *COOH (c-d), *H (e-f) attached, where C atoms in light gray, N atoms in beige, O in red, H in white, Fe in blue, and Ni in black.

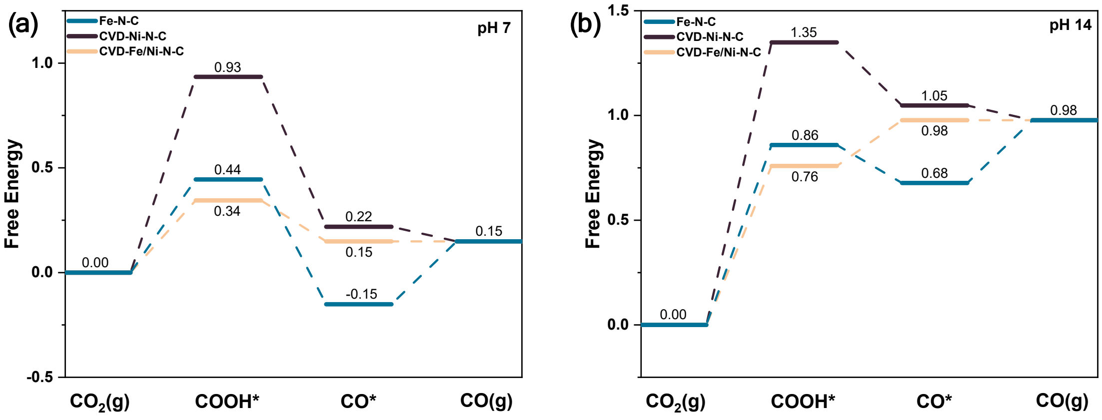

Figure S33. Free energy profile of CO_2 to CO for the Fe-N-C, the CVD-Ni-N-C, and the CVD-Ni/Fe-N-C catalysts at –0.7 V *vs*. SHE with pH= 7 (a) and pH=14 (b).

Notes:

During the CO_2RR, electrode potential and the local pH values directly influence the thermodynamic driving force due to its proton-coupled electron transfer (PCET) steps. The Nernst equation in the energy profiles can explain this.

Nernst equation: $E = E^o - \frac{0.0592}{n} \log Q$

Where Q is dependent on proton and reaction intermediate concentrations (activity). This indicates that pH plays a crucial role in H^+ concentration; lower pH corresponds to a higher H^+ concentration, shifting the potential E to more negative values and vice versa. Thus, the overpotential required for the PCET steps would be decreased.

Furthermore, based on the equation: $\Delta G = -nFE$. Since lower pH values cause a more negative E, hence ΔG becomes more negative (more thermodynamically favorable). As a result, this will alter the reaction pathway and the nature of the rate-determining step. Using the Nernst equation under different pH conditions, assuming at 25 °C (298 K):

$CO_2(g) + H^+ + e^- + * \rightarrow COOH^*$

$COOH^* + H^+ + e^- \rightarrow CO^* + H_2O$

$CO^* \rightarrow CO(g) + *$

The ΔG values at COOH*, CO* adsorption and CO(g) in the CVD-Fe/Ni-N-C at pH=0 were calculated:

$\Delta G\ (COOH*) = -0.07\ eV$

$\Delta G\ (CO*) = -0.68\ eV$

$\Delta G\ (CO_{(g)}) = -0.68\ eV$

Re-arrange to find $E^o = E + 0.0591 \times n \times \text{pH}$

Meanwhile, the corresponding ΔG values on the CVD-Fe/Ni-N-C catalyst at pH=7 are below:

$\Delta G^o\,(COOH*) = -\,0.07 + 0.0592 \times 1 \times 7 = 0.34\,eV$
$\Delta G^o\,(CO*) = -\,0.68 + 0.0592 \times 2 \times 7 = 0.15\,eV$
$\Delta G^o\,(CO_{(g)}) = -\,0.68 + 0.0592 \times 2 \times 7 = 0.15\,eV$

Likewise, the values on the CVD-Fe/Ni-N-C at pH=14 are below:
$\Delta G^o\,(COOH*) = -\,0.07 + 0.0592 \times 1 \times 14 = 0.76\,eV$
$\Delta G^o\,(CO*) = -\,0.68 + 0.0592 \times 2 \times 14 = 0.98\,eV$
$\Delta G^o\,(CO_{(g)}) = -\,0.68 + 0.0592 \times 2 \times 14 = 0.98\,eV$

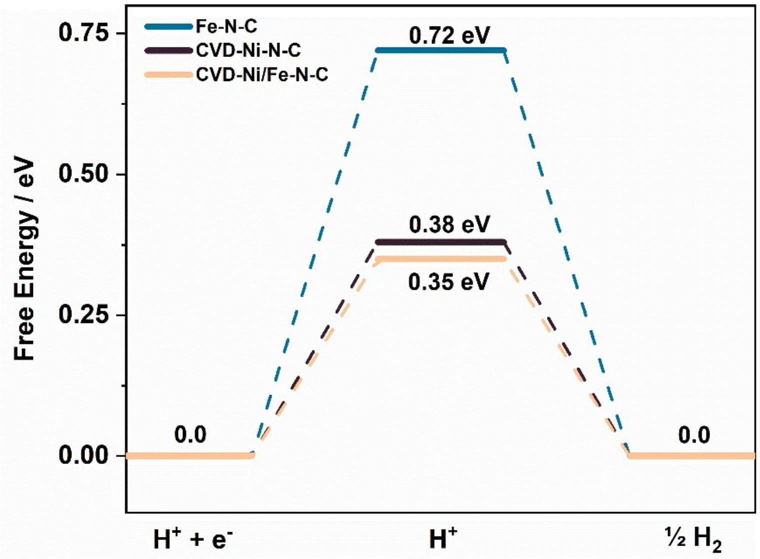

Figure S34. Free energy profile of HER for the Fe-N-C, the CVD-Ni-N-C, and the CVD-Ni/Fe-N-C catalysts.

Additional Tables

Table S1. ICP-OES determined the metal contents of Fe, Ni, and Zn.

Samples	Mass of $Ni(acac)_2$	Fe	Ni	Zn
	mg	at.%	at.%	at.%
Fe-N-C	0.0	18.8	0.0	81.2
CVD-Ni_{11}/Fe_{15}-N-C	4.0	14.7	10.8	74.6
CVD-Ni_{20}/Fe_{17}-N-C	6.7	16.8	20.0	63.2
CVD-Ni_{36}/Fe_{13}-N-C	20.0	13.0	36.4	50.5
CVD-Ni_{82}/Fe_{14}-N-C	**60.0**	**14.4**	**81.7**	**3.9**
CVD-Ni_{66}/Fe_{12}-N-C	100.0	11.7	65.9	22.3
CVD-Ni-N-C	60.0	0.0	76.6	23.4

Table S2. ICP-OES determined the metal contents of Fe, Ni, and Zn.

Samples	Mass of $Ni(acac)_2$	Fe	Ni	Zn
	mg	wt.%	wt.%	wt.%
Fe-N-C	0.0	0.69	-	3.50
CVD-Ni_{11}/Fe_{15}-N-C	4.0	0.70	0.54	4.17
CVD-Ni_{20}/Fe_{17}-N-C	6.7	0.72	0.90	3.17
CVD-Ni_{36}/Fe_{13}-N-C	20.0	0.62	1.82	2.81
CVD-Ni_{82}/Fe_{14}-N-C	60.0	0.69	4.13	0.22
CVD-Ni_{66}/Fe_{12}-N-C	100.0	0.65	3.84	1.45
Ni-N-C	60.0	-	3.83	1.30

Table S3. Summary of the recently reported dual-atom electrocatalysts for CO_2 reduction in H-cell.

Catalyst	**Electrolyte**	**Maximum FE_{CO} (%)**	**Potential (V vs. RHE)**	**J_{co} (mA cm^{-2})**	**Stability**	**Refs.**
CVD-Ni/Fe-N-C	0.5 M $KHCO_3$	98	−0.6	−55	−0.7 V (20 h)	**This work**
Fe_1-Ni_1-N-C	0.5 M $KHCO_3$	96.2	−0.5	−2.4	−0.5 V (10 h)	J. Am. Chem. Soc. 143, 19417-19424 (2021)[26]
Ni/Fe-N-C	0.5 M $KHCO_3$	98	−0.7	−7.4	−0.7 V (30 h)	Angew. Chem. Int. Ed. 58, 6972-6976 (2019)[27]
ZIF-NC-0.5Ni-Fe	0.5 M $KHCO_3$	96.1	−0.7	−10.7	−0.52 V (50 h)	Angew. Chem. Int. Ed. 61, e202205632 (2022)[6]
Fe_2–N_6–C-o	0.5 M $KHCO_3$	95.85	−0.8	~ −24.5	−0.8 V (~21 h)	ACS Energy Lett. 7, 640-649 (2022)[9]
NiCu-NC	0.1 M $KHCO_3$	98	−1.27	−18.2	−1.07 V (30 h)	Adv. Mater. 35, e2209386 (2023)[10]
Ni_2-N_3C_4		98.9	−0.88	~−23	−0.88 V (~30 h)	Angew. Chem. Int. Ed. 61, e202215187 (2022) [28]
Ni_2NC	0.1 M $KHCO_3$	~99	−0.8	~−80	/	Nat. Synth 1, 719-728 (2022)[29]

Table S4. Summary of recently reported Ni-based atomically dispersed electrocatalysts for CO_2 reduction in MEAs and flow cells.

Catalyst	Electrolyte	Type	Maximum FE_{CO} (%)	Potential (V vs. RHE)	J_{co} (mA cm^{-2})	Ref.
CVD-Ni/Fe-N-C	0.1 M $KHCO_3$	MEA	96	−3.8 (Cell voltage)	675	**This work**
CVD-Ni-N-C	0.1 M $KHCO_3$	MEA	91	−3.9 (Cell voltage)	455	**This work**
NiS	0.1 M $CsHCO_3$	MEA	86.9	~3.3 (Cell voltage)	300	Adv. Energy Mater. 2022, 12, 2201843[6]
Ni-ASCs/4.3 wt.%	1.0 M $KHCO_3$	MEA	98.5	3.5 (Cell voltage)	450.3	Adv. Energy Mater. 2022, 12, 2201278[11]
	1 M KOH	Flow cell	95.1	−0.127	507.2	
3D-Ni-SAC	0.1 M $KHCO_3$	MEA	92.5	3.5 (Cell voltage)	400	Nature Synthesis 1, 658-667 (2022)[8]
	1.0 M $KHCO_3$	Flow cell	98.9	−0.87	350	
Ni-N-CNS/CNT-20	1 M KOH	Flow cell	85	−2.0	510	ACS Catal. 11, 10333-10344 (2021)[30]
$Ni-N_4/C-NH_2$	1 M KOH	Flow cell	89.3	−1.0	~450	Energy Environ. Sci. 14, 2349-2356 (2021)[31]
NiPc-OMe MDE	1.0 M $KHCO_3$	Flow cell	99.5	−0.61	-300	Nat. Energy 5, 684-692 (2020)[32]
Ni_2NC	1 M KOH	Flow cell	~99	−0.8	~1000	Nat. Synth 1, 719-728 (2022)[29]
$Ni-N_5-C$	1 M $KHCO_3$	Flow cell	~97	−2.4	1230	Angew Chem Int Ed, e202210985 (2022)[33]

Table S5. Performance comparison of acidic CO_2 electrolysis with atomically dispersed catalysts.

Catalyst	Electrolyte	Type	Maximum FE_{CO} (%)/	J_{co} (mA cm^{-2})	Stability	Refs.
CVD-Ni/Fe-N-C	0.025 M H_2SO_4 + 3 M KCl	Flow cell	95	571	20 h (300 mA cm^{-2})	**This work**
CVD-Ni-N-C			89	445	/	
Ni-N-C	H_2SO_4 +1M Cs_2SO_4	Flow cell	~100	250	36 h (100 mA cm^{-2})	Adv. Mater. 34, 2201295 (2022)[2]
Ni_5@NCN	0.001 M H_2SO_4 + 0.25 M Na_2SO_4	Flow cell	84.3	102	15 h (3.4 V vs.RHE)	ACS Appl. Mater. Inter. 14, 7900-7908 (2022)[34]
NiN-CNTs-500	0.5 M K_2SO_4 + H_2SO_4	Flow cell	96.7	514.0	10 h (100 mA cm^{-2})	ChemSusChem, e202300829 (2023)[35].
NiPc-OMe MDE	0.5 M K_2SO_4 + H_2SO_4	Flow cell	>99	400	12 h (100 mA cm^{-2})	Adv. Energy Mater. 13, 202203603 (2022) [36]
Ni-N-C	0.5 M K_2SO_4 + H_2SO_4	MEA	95	475	20 h (100 mA cm^{-2}) 8 h (500 mA cm^{-2})	Energy Environ. Sci. 16, 1502-1510 (2023) [37]

Table S6. EDS Quantification of the Fe-N-C, the CVD-Ni-N-C, and the CVD-Ni/Fe-N-C catalysts.

Sample	**Fe-N-C**	**CVD-Ni-N-C**	**CVD-Ni/Fe-N-C**
	at.%	at.%	at.%
C	96.22±0.38	94.97±0.46	94.75±0.18
N	1.75±0.24	2.81±0.36	2.48±0.11
O	1.88±0.12	1.76±0.10	2.28±0.14
Fe	0.04±0.01	0.01±0.00	0.06±0.01
Ni	0.00	0.30±0.08	0.38±0.01
Zn	0.11±0.02	0.14±0.05	0.04±0.02

Table S7. XPS elemental contents analysis of prepared samples. All values are provided in terms of the absolute atomic percentage relative to all elements.

Sample	C1s (at. %)	N1s (at. %)	O1s (at. %)	Fe2p (at.%)	Ni2p (at.%)	Zn2p3 (at.%)
CVD-Ni/Fe-N-C	87.70±0.09	8.04±0.04	2.52±0.12	0.82±0.08	0.81±0.02	0.12±0.07
CVD-Ni-N-C	86.83±0.08	8.73±0.05	2.80±0.30	0.00	0.90±0.16	0.06±0.03
Fe-N-C	86.66±0.33	4.97±0.13	8.03±0.25	0.08±0.02	0.00	0.28±0.08

Table S8. Different nitrogen type percentages for the CVD-Ni/Fe-N-C, the CVD-Ni-N-C, and the Fe-N-C from XPS fitting.

Sample	Pyridinic N		M-N		Pyrrolic N		Graphitic N		NO_x	
	at.%	%	at.%	%	at.%	%	at.%	%	at.%	%
CVD-Ni/Fe-N-C	2.5	30.7	1.7	21.6	1.9	23.8	1.2	14.6	14.6	9.3
CVD-Ni-N-C	3.3	38.1	1.3	15.2	2.3	26.2	1.0	11.7	11.7	8.8
Fe-N-C	1.6	31.2	0.8	15.5	1.6	31.4	0.7	13.3	13.3	8.6

Table S9. BET surface area and pore volume of the Fe-N-C, the CVD-Ni-N-C, and the CVD-Ni/Fe-N-C catalysts.

Sample	V_{micro}		V_{meso}		V_{macro}		V_{total}	S_{BET}
	$cm^3\ mg^{-1}$	%	$cm^3\ mg^{-1}$	%	$cm^3\ mg^{-1}$	%	$cm^3\ mg^{-1}$	$m^2\ g^{-1}$
CVD-Ni/Fe-N-C	0.18	40.0	0.14	31.1	0.06	13.3	0.45	541.7
CVD-Ni-N-C	0.14	43.8	0.12	37.5	0.06	18.8	0.32	469.9
Fe-N-C	0.17	54.9	0.09	29.0	0.05	16.1	0.31	516.1

Table S10. Fitting Fe Edge and Ni Edge EXAFS parameters for the CVD-Ni/Fe-N-C catalyst. (CN: coordination number, R: distance between absorber and backscatter atoms, E_0: energy shift, σ^2: Debye-Waller factor (DWF) value, R factor suggests the goodness of fit). The single-digit numbers in parentheses are the last-digit errors except the error in bracket for E_0 as those represent the full errors.

Sample	Scattering Path	CN	R (A)	E_0 (eV)	σ^2 (A^2)	R-factor
Fe Edge CVD-Ni/Fe-N-C 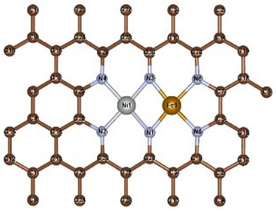	Fe-N	2.5 (4)	1.95 (1)	-2.0 (3.6)	0.007 (2)	0.0078
	Fe-N	2.5 (4)	2.06 (1)		0.007 (2)	
	Fe-Ni	1.2 (2)	2.46 (2)		0.007 (2)	
	Fe-C	2.5 (4)	2.62 (3)		0.0008 (5)	
	Fe-C	2.5 (4)	2.99 (7)		0.03 (2)	
	Fe-C	2.5 (4)	3.06 (7)		0.03 (2)	
	Fe-N-C	5.0 (9)	3.34 (3)		0.002 (3)	
Ni Edge CVD-Ni/Fe-N-C	Ni-N	4.0 (9)	1.87 (3)	-2.0 (1.6)	0.008 (4)	
	Ni-Fe	1.0 (3)	2.46 (2)		0.007 (2)	
	Ni-C	2.0 (5)	2.6 (3)		0.01 (4)	
	Ni-C	4.0 (9)	2.9 (3)		0.02 (9)	
	Ni-N-C	4.0(9)	3.1 (2)		0.003 (9)	

Table S11. Free energy changes upon H* and COOH* adsorption on the Fe-N-C, the CVD-Ni-N-C, and the CVD-Ni/Fe-N-C surfaces at –0.7 V *vs*. RHE. The Unit is eV.

Catalysts	ΔG_{H*}	ΔG_{COOH*}	$\Delta G_{COOH*} - \Delta G_{H*}$
CVD-Ni/Fe-N-C	0.35	–0.07	–0.28
Fe-N-C	0.72	0.03	–0.69
CVD-Ni-N-C	0.38	0.52	–0.17

References

1. Y. Zeng, C. Li, B. Li, J. Liang, M. J. Zachman, D. A. Cullen, R. P. Hermann, E. E. Alp, B. Lavina, S. Karakalos, M. Lucero, B. Zhang, M. Wang, Z. Feng, G. Wang, J. Xie, D. J. Myers, J.-P. Dodelet and G. Wu, *Nature Catalysis*, 2023, **6**, 1215–1227.
2. S. Liu, C. Li, M. J. Zachman, Y. Zeng, H. Yu, B. Li, M. Wang, J. Braaten, J. Liu, H. M. Meyer, M. Lucero, A. J. Kropf, E. E. Alp, Q. Gong, Q. Shi, Z. Feng, H. Xu, G. Wang, D. J. Myers, J. Xie, D. A. Cullen, S. Litster and G. Wu, *Nature Energy*, 2022, **7**, 652-663.
3. Y. Li, W. Shan, M. J. Zachman, M. Wang, S. Hwang, H. Tabassum, J. Yang, X. Yang, S. Karakalos, Z. Feng, G. Wang and G. Wu, *Angew. Chem. Int. Ed.*, 2022, **61**, e202205632.
4. A. I. Frenkel, *Chemical Society Reviews*, 2012, **41**, 8163-8178.
5. Y. Zhao, L. Hao, A. Ozden, S. Liu, R. K. Miao, P. Ou, T. Alkayyali, S. Zhang, J. Ning, Y. Liang, Y. Xu, M. Fan, Y. Chen, J. E. Huang, K. Xie, J. Zhang, C. P. O'Brien, F. Li, E. H. Sargent and D. Sinton, *Nature Synthesis*, 2023, **2**, 403–412.
6. M. H. Han, D. Kim, S. Kim, S. H. Yu, D. H. Won, B. K. Min, K. H. Chae, W. H. Lee and H. S. Oh, *Advanced Energy Materials*, 2022, **12**, 2201843.
7. N. Mohd Adli, W. Shan, S. Hwang, W. Samarakoon, S. Karakalos, Y. Li, D. A. Cullen, D. Su, Z. Feng, G. Wang and G. Wu, *Angew. Chem. Int. Ed.*, 2021, **60**, 1022-1032.
8. Y. Li, N. M. Adli, W. Shan, M. Wang, M. J. Zachman, S. Hwang, H. Tabassum, S. Karakalos, Z.

Feng, G. Wang, Y. C. Li and G. Wu, *Energy & Environmental Science*, 2022, **15**, 2108-2119.

9. Y. Wang, B. J. Park, V. K. Paidi, R. Huang, Y. Lee, K.-J. Noh, K.-S. Lee and J. W. Han, *ACS Energy Letters*, 2022, **7**, 640-649.
10. D. Yao, C. Tang, X. Zhi, B. Johannessen, A. Slattery, S. Chern and S. Z. Qiao, *Adv Mater*, 2023, **35**, e2209386.
11. X. Sheng, W. Ge, H. Jiang and C. Li, *Advanced Materials*, 2022, **34**, 2201295.
12. J. P. Perdew, K. Burke and M. Ernzerhof, *Physical Review Letters*, 1996, **77**, 3865-3868.
13. G. Kresse and J. Furthmüller, *Computational Materials Science*, 1996, **6**, 15-50.
14. G. Kresse and J. Hafner, *Physical Review B*, 1994, **49**, 14251-14269.
15. K. Mathew, V. S. C. Kolluru, S. Mula, S. N. Steinmann and R. G. Hennig, *The Journal of Chemical Physics*, 2019, **151**.
16. K. Mathew, R. Sundararaman, K. Letchworth-Weaver, T. A. Arias and R. G. Hennig, *The Journal of Chemical Physics*, 2014, **140**.
17. G. Kresse and D. Joubert, *Physical Review B*, 1999, **59**, 1758-1775.
18. P. E. Blöchl, O. Jepsen and O. K. Andersen, *Physical Review B*, 1994, **49**, 16223-16233.
19. J. Klimeš, D. R. Bowler and A. Michaelides, *Physical Review B*, 2011, **83**.
20. G. Di Liberto, L. A. Cipriano and G. Pacchioni, *ACS Catalysis*, 2022, DOI: 10.1021/acscatal.2c01011, 5846-5856.
21. L. A. Cipriano, G. Di Liberto and G. Pacchioni, *ACS Catalysis*, 2022, **12**, 11682-11691.
22. Y. Mao, Z. Wang, H.-F. Wang and P. Hu, *ACS Catalysis*, 2016, DOI: 10.1021/acscatal.6b01449, 7882-7891.
23. Z. Wang, X. M. Cao, J. Zhu and P. Hu, *Journal of Catalysis*, 2014, **311**, 469-480.
24. A. A. Peterson, F. Abild-Pedersen, F. Studt, J. Rossmeisl and J. K. Nørskov, *Energy & Environmental Science*, 2010, **3**, 1311-1315.
25. F. Pan, B. Li, E. Sarnello, S. Hwang, Y. Gang, X. Feng, X. Xiang, N. M. Adli, T. Li, D. Su, G. Wu, G. Wang and Y. Li, *Nano Energy*, 2020, **68**, 104384.

26. L. Jiao, J. Zhu, Y. Zhang, W. Yang, S. Zhou, A. Li, C. Xie, X. Zheng, W. Zhou, S. H. Yu and H. L. Jiang, *J Am Chem Soc*, 2021, **143**, 19417-19424.
27. W. Ren, X. Tan, W. Yang, C. Jia, S. Xu, K. Wang, S. C. Smith and C. Zhao, *Angew. Chem. Int. Ed.*, 2019, **58**, 6972-6976.
28. Y. N. Gong, C. Y. Cao, W. J. Shi, J. H. Zhang, J. H. Deng, T. B. Lu and D. C. Zhong, *Angew. Chem. Int. Ed.*, 2022, **61**, e202215187.
29. Q. Hao, H.-x. Zhong, J.-z. Wang, K.-h. Liu, J.-m. Yan, Z.-h. Ren, N. Zhou, X. Zhao, H. Zhang, D.-x. Liu, X. Liu, L.-w. Chen, J. Luo and X.-b. Zhang, *Nature Synthesis*, 2022, **1**, 719-728.
30. Y. Gang, E. Sarnello, J. Pellessier, S. Fang, M. Suarez, F. Pan, Z. Du, P. Zhang, L. Fang, Y. Liu, T. Li, H.-C. Zhou, Y. H. Hu and Y. Li, *ACS Catalysis*, 2021, **11**, 10333-10344.
31. Z. Chen, X. Zhang, W. Liu, M. Jiao, K. Mou, X. Zhang and L. Liu, *Energy & Environmental Science*, 2021, **14**, 2349-2356.
32. X. Zhang, Y. Wang, M. Gu, M. Wang, Z. Zhang, W. Pan, Z. Jiang, H. Zheng, M. Lucero, H. Wang, G. E. Sterbinsky, Q. Ma, Y.-G. Wang, Z. Feng, J. Li, H. Dai and Y. Liang, *Nature Energy*, 2020, **5**, 684-692.
33. J. R. Huang, X. F. Qiu, Z. H. Zhao, H. L. Zhu, Y. C. Liu, W. Shi, P. Q. Liao and X. M. Chen, *Angew. Chem. Int. Ed.*, 2022, DOI: 10.1002/anie.202210985, e202210985.
34. Z. Liu, T. Yan, H. Shi, H. Pan, Y. Cheng and P. Kang, *ACS Appl Mater Interfaces*, 2022, **14**, 7900-7908.
35. Y. Zeng, J. Zhao, S. Wang, X. Ren, Y. Tan, Y. R. Lu, S. Xi, J. Wang, F. Jaouen, X. Li, Y. Huang, T. Zhang and B. Liu, *J Am Chem Soc*, 2023, **145**, 15600-15610.
36. Z. Jiang, Z. Zhang, H. Li, Y. Tang, Y. Yuan, J. Zao, H. Zheng and Y. Liang, *Advanced Energy Materials*, 2022, **13**, 202203603.
37. H. Li, H. Li, P. Wei, Y. Wang, Y. Zang, D. Gao, G. Wang and X. Bao, *Energy & Environmental Science*, 2023, **16**, 1502-1510